PIER Photonics

(Received 30 June 2026, Accepted 30 August 2026, Scheduled 31 August 2026)

β-Ga_2O_3 Polarization-Sensitive Photodetectors: From Materials Fundamentals and Modulation Strategies Toward System Integration

Gang Wu[1,2], Chao Wu[1,2], Qixin Guo[3], Julian Evans[4], and Daoyou Guo[1,2,*]

[1] *Zhejiang-Mexico Joint Laboratory of Intelligent Optoelectronic Sensing, Zhejiang Sci-Tech University, Hangzhou 310018, China*
[2] *Zhejiang Key Laboratory of Quantum State Control and Optical Field Manipulation & Department of Physics Zhejiang Sci-Tech University, Hangzhou 310018, China*
[3] *Department of Electrical and Electronic Engineering, Synchrotron Light Application Center Saga University, Saga 840-8502, Japan*
[4] *Centre for Optical and Electromagnetic Research, National Engineering Research Center for Optical Instruments College of Optical Science and Engineering, Zhejiang University, Hangzhou 310058, China*

ABSTRACT: β-Ga_2O_3 combines solar-blind spectral selectivity, intrinsic crystallographic anisotropy, and ultrawide-bandgap robustness, making it a distinctive platform for ultraviolet polarization photodetection. This review examines how microscopic anisotropy is translated into usable polarization information across the material-device-system hierarchy. We first distinguish anisotropic optical absorption, the monoclinic dielectric tensor, excitonic effects, and direction-dependent carrier transport, emphasizing that these mechanisms are related but not interchangeable. We then assess substrate orientation, strain, doping/alloying, and structural engineering as routes to preserve, reshape, amplify, or introduce polarization selectivity. At the device level, responsivity, detectivity, polarization ratio, response speed, and operating bias are evaluated together with self-powered interface engineering and linear-polarimetric reconstruction, highlighting performance trade-offs and the possibility that interfaces may preserve, amplify, or obscure intrinsic anisotropy. Representative proof-of-concept demonstrations in optical communication, neuromorphic processing, physical unclonable functions, and wavelength-assisted molecular sensing are critically assessed from a system-level perspective. We conclude that future progress depends on establishing quantitative links among microscopic anisotropy, external modulation, interfaces, device readout, and polarization-information fidelity rather than pursuing isolated record metrics.

1. INTRODUCTION

Highly sensitive and interference-resistant optical polarization detection is playing an increasingly critical role in space communication [1–3], environmental monitoring [4–6], intelligent imaging [7–10], and information security [11, 12]. Conventional visible-light polarization systems are susceptible to background noise and scattering interference, and under complex channel conditions, both signal fidelity and detection sensitivity can be substantially degraded [13]. These limitations motivate the development of polarization-sensitive photodetectors in which polarization information can be directly transduced at the device level, while simultaneously maintaining strong spectral selectivity and environmental robustness. Such an approach places particular demands on the active material, which must simultaneously provide polarization discrimination, spectral selectivity, and stable photoconversion.

Against this background, gallium oxide (Ga_2O_3) is a prototypical ultrawide-bandgap oxide semiconductor. Its β-phase possesses a bandgap of approximately 4.9 eV [14–17], a theoretical critical breakdown field as high as ~8 MV/cm [18–20], excellent thermochemical stability [21–23], and compatibility with cost-effective melt-growth techniques [24–26]. These attributes have established β-Ga_2O_3 as an important material platform for power electronics and solar-blind ultraviolet photodetection [27]. For polarization-sensitive photodetection, however, two characteristics are particularly consequential: its ultrawide bandgap provides intrinsic solar-blind spectral selectivity, whereas its low-symmetry crystal structure gives rise to pronounced optical and electrical anisotropy. The solar-blind spectral region (200–280 nm) corresponds to ultraviolet wavelengths that are strongly attenuated by atmospheric ozone, resulting in an extremely low solar background at ground level — a feature that enables high signal-to-noise ratio detection without the need for complex optical filtering [108]. The second characteristic originates from the monoclinic crystal structure of β-Ga_2O_3 (space group C2/m) [28–31], whose low symmetry enables intrinsic polarization-resolved detection through direction-dependent optical and electrical responses without additional polarizing elements. The coexistence of solar-blind spectral selectivity and intrinsic polarization discrimination within a single semiconductor therefore defines a distinctive functional niche for β-Ga_2O_3, particularly for compact ultraviolet polarimetric systems that seek to reduce reliance on external polarization optics [32, 33].

Recent representative advances in polarization-sensitive photodetection have demonstrated the growing importance of

* Corresponding author: Daoyou Guo (dyguo@zstu.edu.cn).

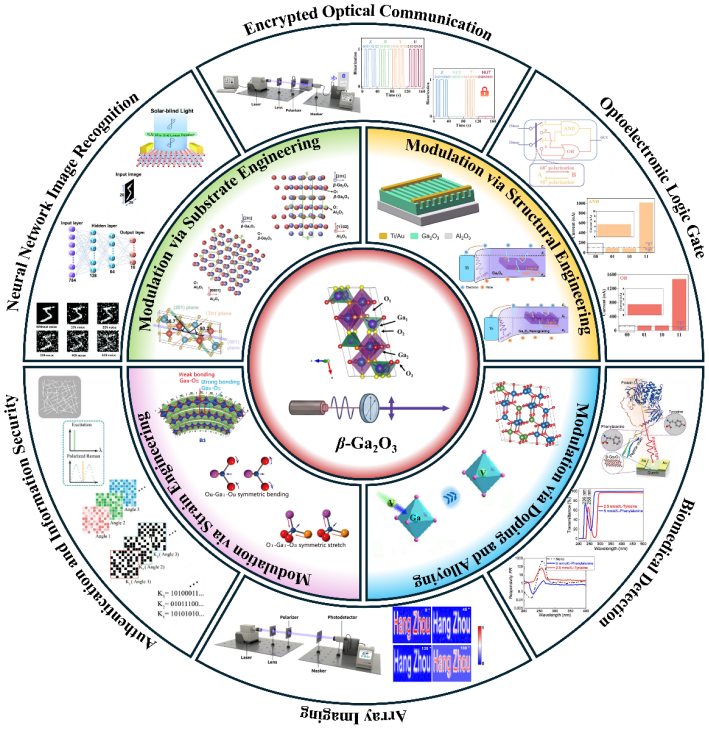

FIGURE 1. Overview of representative modulation strategies and emerging application scenarios for polarization-sensitive β-Ga_2O_3 optoelectronics.

this capability across diverse material platforms and device architectures, including van der Waals heterojunction-based unipolar barrier detectors [111], dispersion-assisted high-dimensional photodetectors for simultaneous full-Stokes polarization and broadband spectrum detection [110], and tunable moiré sensors for spectro-polarimetric imaging [109]. These developments also underscore that β-Ga_2O_3 is not universally superior to other emerging polarization-sensitive platforms. Rather, its particular significance lies in the combination of intrinsic crystallographic anisotropy, solar-blind spectral selectivity, and the robustness associated with an ultrawide-bandgap oxide semiconductor.

Nevertheless, research on polarization-sensitive β-Ga_2O_3 optoelectronics is expanding rapidly but still faces several fundamental and technological challenges. Despite substantial improvements in individual device metrics, the central challenge of the field is no longer simply how to obtain a larger polarization ratio, but how to translate the intrinsic microscopic anisotropy of β-Ga_2O_3 into reproducible and controllable device responses that ultimately support reliable system-level polarization information. At the materials level, quantitative links among crystal orientation, dielectric response, polarization-dependent absorption, and carrier transport remain incomplete. At the modulation level, substrate orientation, strain, doping, and nanostructuring can alter the measured anisotropy, yet their coupled mechanisms and practical performance limits are not fully established. At the device level, interfaces and heterojunctions introduce additional carrier separation, trapping, and contact effects that may preserve, amplify, or partially obscure the intrinsic anisotropic response. Finally, at the system level, high polarization ratios measured in individual devices do not automatically guarantee accurate polarization reconstruction, array uniformity, self-powered operation, or robust performance under realistic operating conditions. Together, these challenges indicate that the multiscale correlation between the microscopic anisotropy of β-Ga_2O_3 and its macroscopic device polarization response has yet to be systematically established, leaving a critical gap between material-level anisotropy and practically usable polarization information.

The literature survey was conducted using the Web of Science Core Collection with search terms including "β-Ga_2O_3", "anisotropy", and "polarization photodetector", primarily covering publications from January 2020 to April 8, 2026, along with earlier foundational studies. Representative works were selected to cover four key stages of the anisotropy-to-information pathway established in this review: the microscopic origin of anisotropy, external modulation mechanisms, device- and interface-level polarization transduction, and system-level information extraction. Particular attention was given to studies that provide mechanistic insight or enable meaningful comparison across these stages, while reported performance metrics were evaluated in the context of their measurement conditions rather than on record values alone.

Accordingly, this review examines β-Ga_2O_3 polarization optoelectronics from an anisotropy-to-information perspective, organizing materials physics, modulation strategies, device architectures, and applications as successive stages through which intrinsic anisotropy is translated into usable polarization information. We begin with the crystal structure and plane selection, critically examining the anisotropic optical constants and dielectric tensor characteristics of different crystal phases

and planes, and analyzing the polarization-dependent carrier transport behavior to establish the microscopic origin of polarization discrimination in β-Ga_2O_3. Subsequently, we assess how external perturbations tune, enhance, or potentially compromise the polarization response of β-Ga_2O_3 by focusing on four mainstream modulation strategies: substrate orientation, mechanical strain, doping/alloying, and micro-/nanostructure engineering. On this basis, we evaluate the translation of material anisotropy into device performance by comparing key metrics including responsivity, detectivity, polarization ratio, response speed, and operating bias, while paying particular attention to self-powered operation, heterointerface engineering, and array integration. In particular, heterojunction and contact strategies are discussed in terms of whether they preserve, amplify, or obscure the intrinsic anisotropic response of β-Ga_2O_3. Finally, we critically assess system-level demonstrations based on β-Ga_2O_3 polarization optoelectronic devices in emerging fields such as encrypted communication, neuromorphic vision, physical unclonable function anti-counterfeiting, and biosensing, with emphasis on whether device-level polarization responses can be translated into reliable information under realistic operating conditions. A visual overview of the representative modulation strategies and emerging application scenarios discussed in this review is provided in Fig. 1. We then identify future research priorities based on the fundamental and technological gaps revealed across these stages. Through this framework, we aim to identify where anisotropy is generated, tuned, preserved, amplified, or lost across the material-device-system hierarchy, thereby clarifying the key scientific questions and design priorities required to move β-Ga_2O_3 polarization optoelectronics beyond isolated performance records toward reliable polarization-information technologies.

2. PHYSICAL FUNDAMENTALS OF POLARIZATION PROPERTIES IN β-Ga_2O_3

The polarization properties of β-Ga_2O_3 originate primarily from its low-symmetry monoclinic crystal structure, which gives rise to direction-dependent electronic transitions, dielectric response, and carrier transport. Crystal phase and facet orientation determine how this intrinsic anisotropy is manifested experimentally, whereas the dielectric tensor governs polarization-dependent light propagation and absorption, and anisotropic carrier transport influences the subsequent conversion of photogenerated carriers into electrical signals. These mechanisms are physically related through the underlying crystal symmetry but should not be regarded as interchangeable manifestations of polarization sensitivity. This section therefore establishes the material-level basis of the anisotropy-to-information pathway from three complementary perspectives: crystal phase and facet selection, optical constants and the dielectric tensor, and direction-dependent carrier transport. Extrinsic polarization selectivity introduced by artificial structures, such as subwavelength gratings, is treated separately in Section 3 because its physical origin lies in electromagnetic boundary conditions rather than in the intrinsic crystallographic anisotropy of β-Ga_2O_3.

2.1. Crystal Phase and Facet Selection

Research on the polarization properties of Ga_2O_3 has predominantly focused on the thermodynamically stable β-phase. β-Ga_2O_3 crystallizes in a monoclinic structure (space group C2/m) with lattice constants $a = 12.214$ Å, $b = 3.037$ Å, $c = 5.798$ Å, and $\beta = 103.83°$ [34–37]. Its unit cell contains tetrahedrally and octahedrally coordinated Ga sites, and the crystallographic b-axis coincides with the twofold symmetry axis of the monoclinic lattice. This reduced symmetry removes the equivalence among different crystallographic directions and permits direction-dependent optical transitions, dielectric responses, and lattice-vibrational selection rules. At the electronic level, symmetry-dependent dipole-allowed transitions from different valence bands to the conduction-band minimum produce distinct dielectric responses for different polarization directions; experimentally, this is reflected in polarization-dependent absorption edges and optical bandgaps. At the vibrational level, the C2/m symmetry defines distinct A_g and B_g Raman-active modes whose measured intensities depend on the crystal orientation and polarization geometry [40]. Thus, facet-dependent optical and Raman responses should be regarded as experimentally accessible manifestations of the same underlying low-symmetry lattice, while their magnitudes and selection rules depend on the specific measurement geometry.

For clarity, the crystallographic, Cartesian, optical, and device-direction conventions used throughout this review are distinguished as follows. Crystallographic directions are denoted by [uvw] and planes by (hkl) in the monoclinic lattice with axes a, b, and c. Because the a and c axes are not orthogonal, they should not be treated as a Cartesian pair. When tensor components are expressed in a Cartesian basis, we adopt $x//a$, $y//b$, and $z = x \times y$, following the convention commonly used for the monoclinic dielectric tensor. The dielectric principal axes are labeled as X, Y, and Z, where Y coincides with the b-axis (the twofold symmetry axis), and X and Z lie in the (010) plane and generally do not coincide with fixed crystallographic axes; their orientations vary with photon energy because of the dispersive off-diagonal dielectric-tensor component. When discussing optical polarization, E denotes the electric-field vector of incident light, with $E//b$ and $E//c$ indicating polarization parallel to the respective crystallographic axes. The light-propagation direction is specified explicitly for each measurement geometry rather than being assumed to coincide with a particular crystal axis. For device discussions, the channel direction refers to the orientation of the current path between electrodes. These conventions apply throughout the following sections unless explicitly stated otherwise.

Mu et al. [34] systematically compared the polarized transmittance spectra of three principal planes of β-Ga_2O_3. Among them, the (100) plane exhibited the most pronounced polarization-dependent absorption-edge shift: the ultraviolet cutoff edges for $E//c$ and $E//b$ were located at 276.1 nm and 261.8 nm, corresponding to optical bandgaps of 4.48 eV and 4.73 eV, respectively, yielding a bandgap difference as large as 0.25 eV. The transmittance intensity as a function of the polarization angle was well described by the relation $T(\varphi) = T_{E//b} \sin^2 \varphi + T_{E//c} \cos^2 \varphi$, producing a characteristic

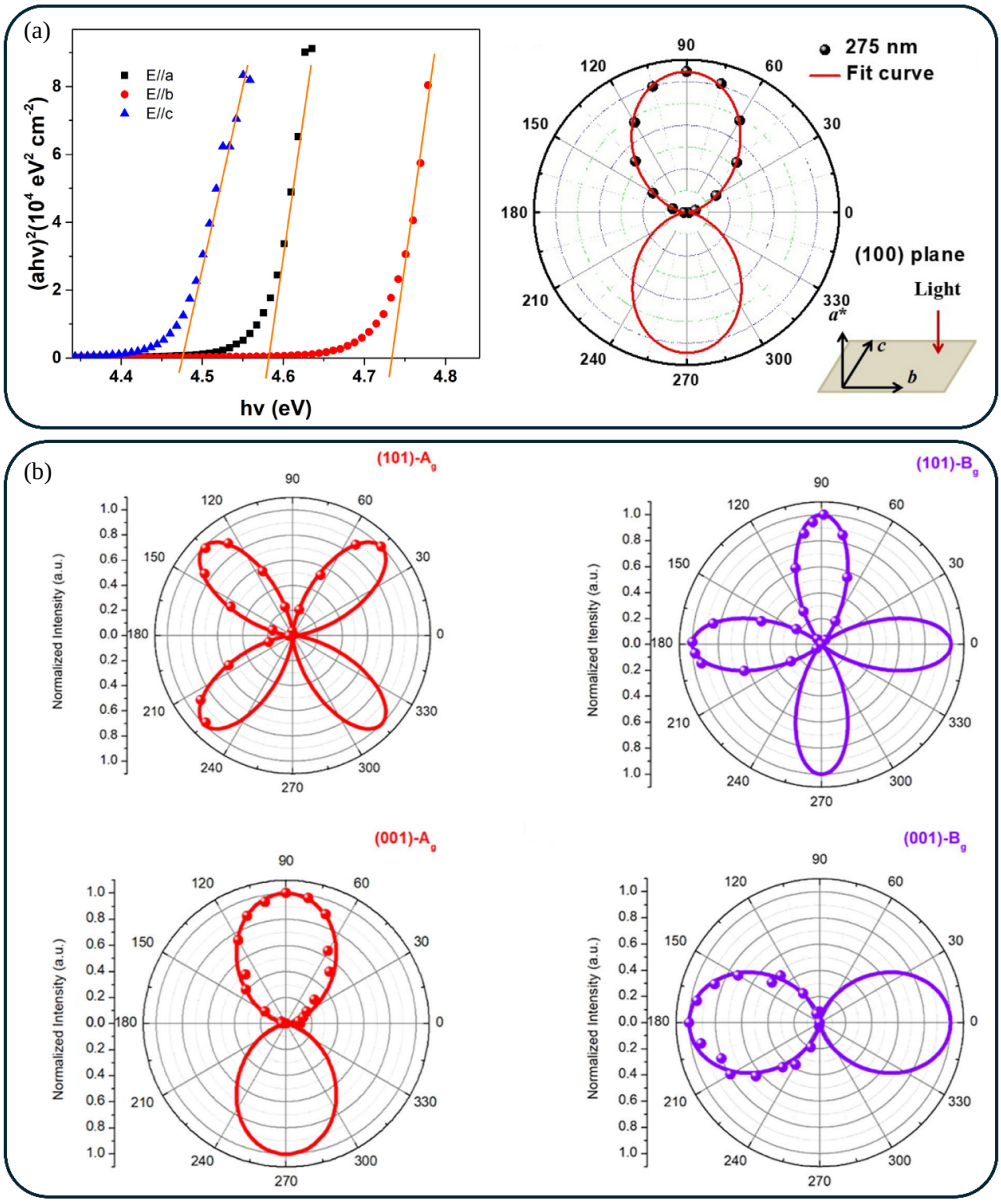

FIGURE 2. Facet-dependent optical and Raman anisotropy of β-Ga_2O_3. (a) Polarization-dependent optical bandgaps and angular transmittance of the (100) β-Ga_2O_3 single crystal. The optical bandgaps for $E//c$ and $E//b$ are 4.48 and 4.73 eV, respectively, corresponding to a 0.25 eV polarization-dependent splitting, while the transmittance at 275 nm exhibits a characteristic two-lobed angular response [34]. *Copyright 202, Elsevier*. (b) Angle-resolved polarized Raman intensity patterns of the (101)- and (001)-oriented β-Ga_2O_3 crystals, showing four-lobed (π/2-periodic) and two-lobed (π-periodic) responses, respectively [39]. *Copyright 2023, American Chemical Society*. Together, these results illustrate that crystal-facet orientation strongly influences both the magnitude and angular form of the experimentally observed optical and vibrational anisotropy in β-Ga_2O_3.

dumbbell-shaped pattern in polar coordinates (Fig. 2(a)). By comparison, the polarized cutoff edges of the (010) and (001) planes showed much smaller separations, indicating substantially weaker in-plane optical discrimination under the corresponding measurement geometries. A different situation was reported for epitaxial $(\bar{2}01)$-oriented β-Ga_2O_3 films. Zhao et al. [38] determined the anisotropic optical constants of a $(\bar{2}01)$-oriented β-Ga_2O_3 thin film by spectroscopic ellipsometry. Owing to the presence of six in-plane rotational domains in the epitaxial film, the intrinsic biaxial optical response was treated using an effective uniaxial model. Its pseudo-ordinary component, associated with the *b*-axis, and pseudo-extraordinary component, associated with the *ac* plane, exhibited optical bandgaps of 4.92 ± 0.02 eV and 4.57 ± 0.02 eV, respectively, corresponding to a difference of approximately 0.35 eV. However, this 0.35 eV separation should not be directly ranked against the 0.25 eV splitting measured for the bulk (100) crystal, because the two values arise from different sample forms, polarization geometries, and optical models. Instead, the result demonstrates that pronounced polarization-dependent optical response can be retained in an epitaxial geometry compatible with thin-film integration. Fu et al. [39] further compared the structural anisotropy of the (101) and (001) planes from the viewpoint of

TABLE 1. Comparison of representative facet-dependent optical, surface, and vibrational characteristics of β-Ga_2O_3.

Parameters	(100) plane	(010) plane	(001) plane	(101) plane	($\bar{2}$01) plane
Unpolarized optical bandgap (eV)	4.70	4.55	4.70	4.70	4.94
Bandgap for $E//c$ (eV)	4.48	~4.55	~4.70	–	4.57
Bandgap for $E//b$ (eV)	4.73	~4.55	~4.70	–	4.92
Surface barrier height Φ_{surf} (eV)	1.30	1.25	1.30	1.12	1.19
In-plane Raman intensity periodicity	90° ($\pi/2$)	–	180° (π)	90° ($\pi/2$)	180° (π)

surface atomic configuration and contact characteristics. The (101) plane is terminated by Ga or O atoms, and its surface dangling bond density was calculated to be approximately one to two times that of the (001) surface, depending on the termination configuration. In angle-resolved polarized Raman spectroscopy (ARPRS), the Raman intensity polar patterns of the (101) plane displayed a four-lobed angular dependence with a period of $\pi/2$, whereas those of the (001) plane exhibited a two-lobed response with a period of π (Fig. 2(b)). Because both A_g and B_g Raman-active modes are governed by the C2/m Raman tensors, their measured angular dependence changes with the projection of these tensors onto the polarization geometry of each crystal plane. The contrasting four- and two-lobed patterns therefore provide a direct experimental signature of facet-dependent Raman anisotropy rather than evidence for a universally superior crystal orientation.

Based on the comparative analysis in Table 1, no single β-Ga_2O_3 crystal orientation can be regarded as universally optimal for polarization-sensitive optoelectronics; instead, facet selection involves application-dependent trade-offs among optical anisotropy, surface electronic properties, contact formation, and integration geometry. The (100) plane offers a significant polarization-dependent bandgap difference of 0.25 eV between $E//b$ and $E//c$, together with a pronounced angular modulation of deep-ultraviolet transmittance, making it particularly favorable when strong intrinsic optical polarization discrimination is the primary design objective ($\bar{2}$01) oriented epitaxial film also exhibits a large pseudo-ordinary/pseudo-extraordinary bandgap separation (~0.35 eV); however, because this value is extracted using an effective uniaxial model for a multidomain thin film, it should not be directly ranked against the bulk-crystal values. Its main practical significance lies in demonstrating that substantial optical anisotropy can be retained in an epitaxial thin-film configuration. The (101) plane features a higher surface dangling-bond density and a lower measured surface barrier than the (001) plane, accompanied by more favorable Ohmic-contact behavior; these characteristics may benefit carrier extraction, although their impact on polarization-resolved detector speed or sensitivity must be evaluated at the device level rather than inferred from surface properties alone. In contrast, the (010) and (001) planes exhibit relatively weak in-plane optical polarization discrimination under the measurement geometries compared here, while the (001) plane exhibits distinct surface/contact characteristics and Raman anisotropy that may be advantageous for other device requirements. Thus, crystal-facet selection should be guided by the specific function to be optimized — optical polarization contrast, interface/contact quality, epitaxial compatibility, or device integration — rather than by a single anisotropy metric.

Beyond oriented single crystals, measurable polarization sensitivity has also been demonstrated in polycrystalline β-Ga_2O_3 thin films. Liu et al. [41] fabricated a plasma-enhanced chemical vapor deposition (PECVD)-grown polycrystalline β-Ga_2O_3 photodetector and observed four-lobed angular patterns in angle-resolved polarized Raman spectroscopy. Under 255 nm linearly polarized illumination, the device exhibited a photocurrent polarization ratio of approximately 1.3. This result indicates that macroscopic polarization discrimination can survive in a non-single-crystalline film; however, the relatively modest polarization ratio and the presence of preferred crystallographic orientations suggest that grain texture and orientation distribution must be considered when interpreting the measured anisotropy. Thus, polycrystalline β-Ga_2O_3 may offer a more scalable route to polarization-sensitive devices, but its anisotropy cannot be assumed to be equivalent to that of a well-defined single-crystal facet.

Other Ga_2O_3 polymorphs and related corundum-phase alloys further broaden the available anisotropy landscape, although the maturity and interpretation of the available evidence vary substantially. Earlier studies on rotationally twinned films commonly described as ε-Ga_2O_3 reported pseudo-ordinary and pseudo-extraordinary optical bandgaps of 4.85 and 4.76 eV, respectively [38]. More recent measurements on single-domain orthorhombic κ-Ga_2O_3 resolved its intrinsic biaxial response more explicitly, revealing fundamental interband transitions at 5.09 eV for ε_{xx}, 4.82 and 5.75 eV for ε_{yy}, and 5.43 eV for ε_{zz} [42]. The distinction between multidomain and single-domain samples is important because rotational domains can partially average the in-plane optical anisotropy, making direct comparison of reported ε/κ-Ga_2O_3 anisotropy values inappropriate without considering domain structure and optical modeling. In addition, m-plane α-$(AlxGa_{1-x})_2O_3$ epilayers exhibit anisotropic surface growth, crystallographic characteristics, and polarization-dependent optical transmission; optical anisotropy has been directly observed for α-Ga_2O_3 and low-Al-composition alloys [43]. These results demonstrate that polarization-related anisotropy is not unique to β-Ga_2O_3, but device-level polarization discrimination in these alternative phases remains far less established. They should therefore be viewed as emerging comparative platforms rather than mature

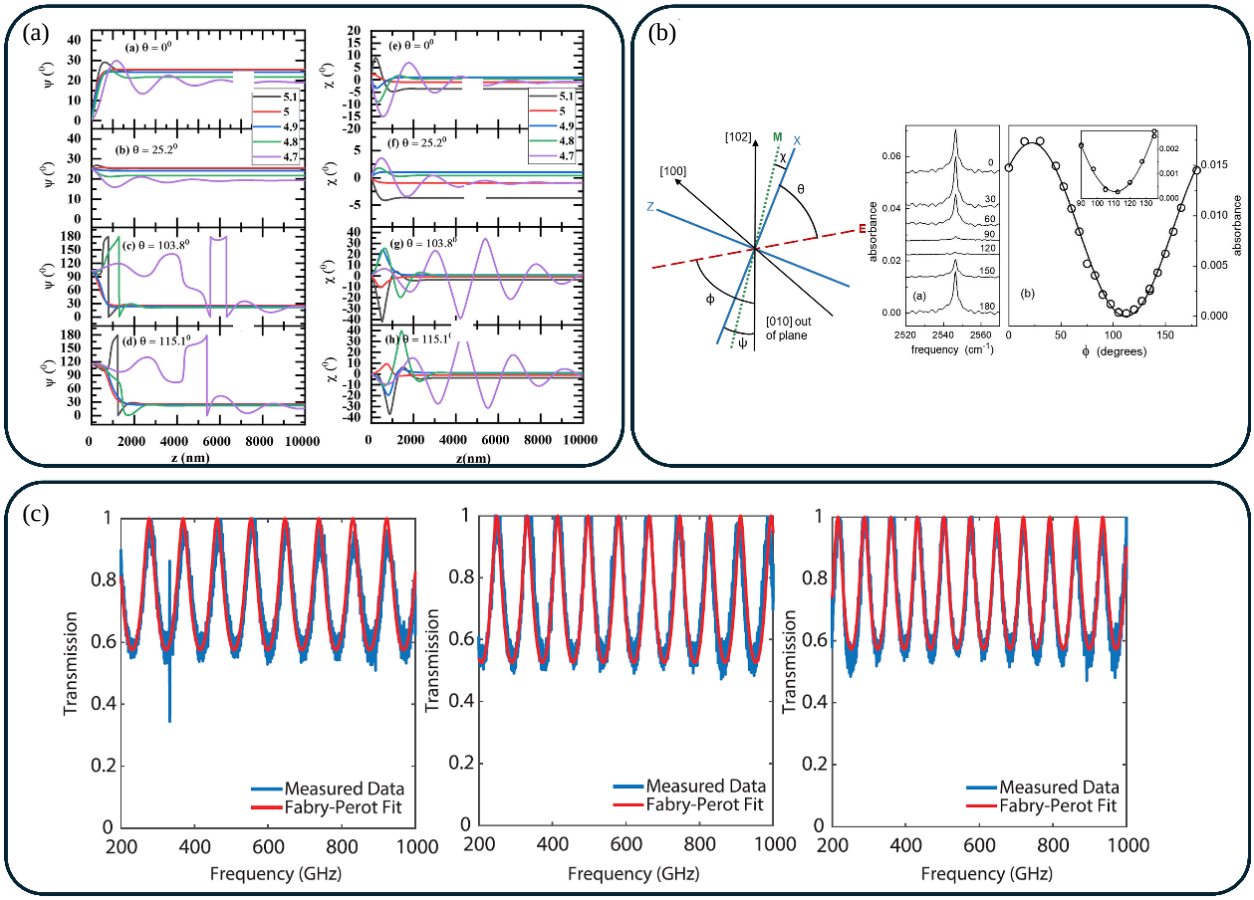

FIGURE 3. Dielectric-axis determination and polarization-dependent optical propagation in β-Ga_2O_3. (a) Depth-dependent evolution of the linear-polarization azimuth and ellipticity for light propagating in the *a*-*c* (010) plane. The polarization progressively approaches the least absorbing X_a-exciton direction ($\sim$20°–25° from the *a*-axis), while birefringence introduces a transient ellipticity during propagation [47]. *Copyright 2024*, *AIP Publishing*. (b) Geometrical definition of the crystallographic axes, principal dielectric axes (X and Z), transition-dipole moment, and analyzer polarization, together with the polarization-dependent O-D vibrational absorption used to determine the dielectric-axis orientation in the near-infrared [50]. *Copyright 202*, *AIP Publishing*. (c) Polarized THz transmission spectra for $E//a^*$, $E//c$, and $E//b$, where the distinct Fabry-Perot fringe spacings reveal the anisotropic quasi-static dielectric response [51]. *Copyright 202*, *AIP Publishing*. Together, these results illustrate how the monoclinic dielectric anisotropy of β-Ga_2O_3 governs both the orientation of its principal dielectric axes and the evolution of polarization during propagation across different spectral regimes.

alternatives to β-Ga_2O_3 for polarization-sensitive photodetection.

2.2. Optical Constants, Dielectric Tensor, and Anisotropic Propagation

The low symmetry of β-Ga_2O_3 dictates that its optical anisotropy must be described by the full dielectric function tensor rather than by a scalar dielectric constant or a simple uniaxial model [44, 45]. In the Cartesian coordinate system defined in Section 2.1, the monoclinic symmetry constrains the complex dielectric tensor to

$$\varepsilon = \begin{pmatrix} \varepsilon_{xx} & 0 & \varepsilon_{xz} \\ 0 & \varepsilon_{yy} & 0 \\ \varepsilon_{xz} & 0 & \varepsilon_{zz} \end{pmatrix} \tag{1}$$

which contains four independent complex-valued components. The off-diagonal term ε_{xz} is a direct consequence of the monoclinic symmetry and couples the optical response within the *x*-*z* plane. Importantly, the diagonal and off-diagonal components exhibit different spectral dispersions, so the dielectric principal axes in this plane are not fixed to the crystallographic axes but rotate with photon energy. Although ε_{xz} is small in the transparent region, it becomes appreciable near and above the absorption edge, where its influence on polarization-dependent absorption and propagation can no longer be neglected. Thus, the optical anisotropy of β-Ga_2O_3 is not adequately characterized by comparing refractive indices or absorption coefficients along a few fixed crystal directions alone; its polarization response must instead be interpreted within the full, frequency-dependent dielectric-tensor framework.

To experimentally determine the orientation of the dielectric principal axes at a specific photon energy, Portoff et al. [50] used the polarization-dependent infrared absorption of the $V_{Ga(1)}$-2D defect as an independent probe. Using the O-D stretching vibration at 2546 cm^{-1} the absorbance was measured as a function of analyzer angle for light propagating along

TABLE 2. Representative optical constants and dielectric parameters of β-Ga_2O_3 along selected directions in different spectral regimes.

Parameter	a-axis	b-axis	c-axis
High-frequency dielectric constant ε_∞	3.46	3.60 ± 0.06	3.54 ± 0.02
Quasi-static dielectric constant ε_s (THz)	10.19 ± 0.03	10.60 ± 0.03	12.27 ± 0.06
Terahertz refractive index n	3.165 ± 0.005	3.231 ± 0.005	$\sim$3.6
Visible-NIR refractive index n	$\sim$1.86	1.96 ± 0.02	1.95 ± 0.02

[010]. The maximum absorbance occurred when the analyzer direction was $22° \pm 3°$ from [102], identifying the X principal dielectric axis at this frequency; equivalently, the Z axis was oriented at $-18° \pm 3°$ relative to [100] (Fig. 3(b)). Through dichroic ratio analysis, the transition dipole moment of the O-D vibration was further found to be oriented at $15° \pm 4°$ relative to [102], consistent with the corresponding density functional theory (DFT) predictions [50]. Importantly, these angles characterize the dielectric-axis orientation near 2546 cm^{-1} and should not be interpreted as frequency-independent crystallographic directions, because the X and Z dielectric axes rotate within the (010) plane as the dielectric tensor disperses with photon energy [44, 50]. Thus, Fig. 3(b) provides an experimental illustration of the distinction between crystallographic axes, dielectric principal axes, and transition-dipole directions that is essential for interpreting polarization-dependent optical measurements in monoclinic β-Ga_2O_3.

The magnitude and even the sign of the dielectric anisotropy vary substantially across the optical-to-terahertz spectrum. Unuma et al. [49] demonstrated this evolution using polarization-resolved transmission spectroscopy on an undoped (100) β-Ga_2O_3 single crystal. In the visible and near-infrared regions, the crystal remains highly transparent and exhibits only weak birefringence, with $n_c - n_b \approx -0.01$. As the photon frequency decreases into the mid- and far-infrared, pronounced polarization-dependent stopbands emerge in the 154–800 cm^{-1} range, consistent with Reststrahlen bands associated with anisotropic optical-phonon resonances. On the low-frequency side of these resonances, the refractive indices increase substantially; near 1 terahertz (THz), $n_b \approx 3.3$ and $n_c \approx 3.6$, yielding $n_c - n_b \approx 0.3$. Thus, the THz birefringence is approximately 30 times larger than its visiblenear-infrared value and has the opposite sign [49]. This spectral evolution indicates that the observed anisotropy changes not only in magnitude but also in physical origin: electronic contributions dominate the weak high-frequency birefringence, whereas the off-resonant response of anisotropic optical phonons strongly enhances the low-frequency dielectric response.

The low-frequency limit was quantified more directly by Gopalan et al. [51] using polarization-resolved THz transmission and generalized spectroscopic ellipsometry. In the measured THz range, no appreciable dispersion of the real permittivity was observed, allowing the response to be treated as quasi-static. The principal dielectric directions were found to lie very close to ($a^\wedge$), b, and c, with THz-GSE permittivities of approximately $\varepsilon_{a^*} = 10.19$, $\varepsilon_b = 10.6$, and $\varepsilon_c = 12.27$ [51]. The polarized transmission spectra in Fig. 3(c) show distinct Fabry-Perot fringe spacings for $E//a^*$, $E//c$, and $E//b$, providing a direct experimental visualization of this low-frequency dielectric anisotropy. Together with the frequency-dependent dielectric-axis orientation discussed above, these measurements show that both the magnitude and the relevant principal directions of the dielectric response must be specified when modeling polarization-dependent electromagnetic propagation in β-Ga_2O_3. Representative dielectric constants and refractive indices obtained across different spectral regimes are summarized in Table 2, providing a quantitative reference for connecting the frequency-dependent dielectric response to optical propagation and device-level electromagnetic modeling. Because the dielectric principal axes of monoclinic β-Ga_2O_3 are generally frequency dependent, the tabulated parameters should be interpreted together with their corresponding spectral range and directional definitions rather than as a single frequency-independent dielectric description.

Near the absorption edge, the tensorial optical response manifests directly as a depth-dependent evolution of the polarization state. Adnan et al. [47] showed that this behavior results from the combined effects of linear dichroism and birefringence. Linear dichroism preferentially attenuates the electric-field component along the more strongly absorbing direction, progressively shifting the orientation of the remaining linear polarization toward the least absorbing excitonic transition. Birefringence, in contrast, introduces a relative phase delay between the polarization components and therefore generates ellipticity during propagation [47, 48]. In the a-c (010) plane, the polarization azimuth ψ evolves toward approximately 20°–25° from the a-axis as the propagation depth approaches $\sim$10 μm, closely matching the transition-dipole direction of the X_a exciton ($\sim$25.2°) and identifying it as the least absorbing direction over the relevant near-edge energy range (Fig. 3(a)). At the same time, the ellipticity parameter χ departs from zero after light enters the crystal because of birefringence; for photon energies around 4.8–5.0 eV, χ becomes small again at larger depths, so the transmitted field approaches a predominantly linear state oriented near the X_a direction. Thus, Fig. 3(a) demonstrates that polarization-dependent absorption in β-Ga_2O_3 cannot be regarded as a fixed surface response: the polarization state itself evolves with propagation depth through the coupled action of excitonic dichroism and birefringence.

The depth-dependent evolution of the polarization state has a direct consequence for optical-absorption modeling. By solving the full electromagnetic wave equation using the measured complex dielectric tensor, Adnan et al. [46] showed that the conventional Beer-Lambert law is not generally valid near

the absorption edge of monoclinic β-Ga_2O_3. In the energy ranges of approximately 4.65–5.2 eV for the (010) plane and 4.9–5.8 eV for the (001) plane, the photon-flux decay requires two effective exponential components rather than a single absorption coefficient. An anisotropic Beer-Lambert description was therefore introduced: the photon flux initially decays with an effective coefficient α until a polarization- and energy-dependent critical depth z_c is reached, beyond which the coefficient approaches α^*, corresponding to the least absorbing polarization direction [46, 47].

This behavior originates from the coupled effects of linear dichroism and birefringence discussed above. Dichroism progressively drives the surviving polarization toward the least absorbing excitonic direction, while birefringence introduces a depth-dependent ellipticity; z_c is closely associated with this polarization-state evolution [47]. At photon energies sufficiently above the absorption edge (> 5.2 eV for the (010) plane and > 5.8 eV for the (001) plane), a single effective absorption coefficient again provides a reasonable approximation [46]. Because the local photocarrier-generation rate depends on the depth-dependent photon flux, this anisotropic absorption behavior provides an important link between intrinsic optical anisotropy and polarization-dependent device response.

While crystal symmetry and dielectric anisotropy govern the polarization-dependent absorption and propagation of light, the conversion of these optical differences into measurable electrical signals further depends on the direction-dependent transport of photogenerated carriers, as discussed in Section 2.3.

2.3. Crystallographic Anisotropy of Carrier Transport

In contrast to the pronounced optical anisotropy, the intrinsic electron-transport anisotropy of β-Ga_2O_3 is relatively weak. Early measurements reported large directional differences in Hall mobility [52], but subsequent studies showed that such variations can be strongly affected by structural defects and growth-related factors [53, 56]. First-principles calculations yielded room-temperature intrinsic electron drift mobilities of 129, 146, and 144 $cm^2V^{-1}s^{-1}$ along the x, y, and z directions, respectively, with an anisotropy below 15%, consistent with the nearly isotropic electron effective mass ($m^* \approx 0.28m_0$) [54, 55]. Moreover, acoustic-phonon scattering contributes appreciably to intrinsic electron transport; neglecting it and considering only polar optical phonon scattering can overestimate the room-temperature mobility by approximately 1.7–2.3 times [54].

A different picture emerges for nonequilibrium photoexcited carriers. Jiang et al. [58] analyzed the three-dimensional momentum, group-velocity, relaxation-time, and mean-free-path distributions in β-Ga_2O_3. Although the initial group-velocity distributions of both electrons and holes are concentrated mainly along [010], their optimal transport directions differ: electrons preferentially transport near [100], whereas holes retain an optimal direction along [010]. The longer relaxation times and mean free paths of holes further indicate more favorable ballistic transport than for electrons near the band edge. These results show that anisotropy in photoexcited-carrier transport can be considerably stronger than that inferred from equilibrium electron mobility alone.

These results highlight an important distinction between optical and transport anisotropy in β-Ga_2O_3. The relatively weak intrinsic electron-mobility anisotropy indicates that a large polarization-dependent photocurrent should not automatically be attributed to direction-dependent electrical transport; anisotropic optical absorption can instead constitute a dominant contribution to the measured polarization response. Nevertheless, the direction-dependent transport of photoexcited carriers can influence their subsequent collection, particularly in nanoscale active regions. Thus, crystal and channel orientations should be considered together when translating intrinsic optical anisotropy into an electrical polarization signal.

3. MODULATION STRATEGIES FOR POLARIZATION PERFORMANCE

While the intrinsic anisotropy of β-Ga_2O_3 is fixed by its monoclinic crystal symmetry, its experimentally accessible polarization response can be substantially modified by external engineering. Importantly, these strategies act through different physical pathways: substrate orientation controls whether intrinsic anisotropy is preserved or averaged during heteroepitaxy, strain and chemical modification perturb the underlying electronic and lattice responses, whereas micro-/nanostructures can further reshape light-matter interaction or introduce extrinsic polarization selectivity. Accordingly, this section discusses four representative modulation strategies: substrate and orientation engineering, strain engineering, doping and alloying, and structural engineering.

3.1. Substrate Engineering and Orientation Control

Substrate engineering modulates the observable anisotropy of heteroepitaxial β-Ga_2O_3 primarily by controlling epitaxial orientation and rotational-domain populations. High-symmetry substrate surfaces can promote multiple rotational variants that partially average the intrinsic in-plane anisotropy, whereas lower-symmetry orientation relationships can reduce this rotational degeneracy and preserve a net anisotropic response [35, 59]. In addition, substrate-dependent lattice mismatch influences anisotropic strain relaxation and defect formation [60]. Thus, substrate selection affects polarization sensitivity through the coupled control of crystal orientation, domain distribution, and crystalline quality.

Zhang et al. [35] demonstrated that substrate orientation can preserve or suppress the intrinsic in-plane anisotropy of heteroepitaxial β-Ga_2O_3 by controlling its crystallographic orientation and rotational-domain population. Pole-figure analysis showed that the film grown on c-plane sapphire forms six rotational variants, whereas growth on r-plane sapphire reduces the rotational degeneracy to four variants because of the different substrate symmetry and interfacial atomic arrangement (Fig. 4(a)). The resulting r-plane-sapphire-grown film exhibits pronounced anisotropic absorption and a polarization ratio of 6.02 under 254 nm illumination, whereas the corresponding c-plane-sapphire-grown film is nearly polarization insensi-

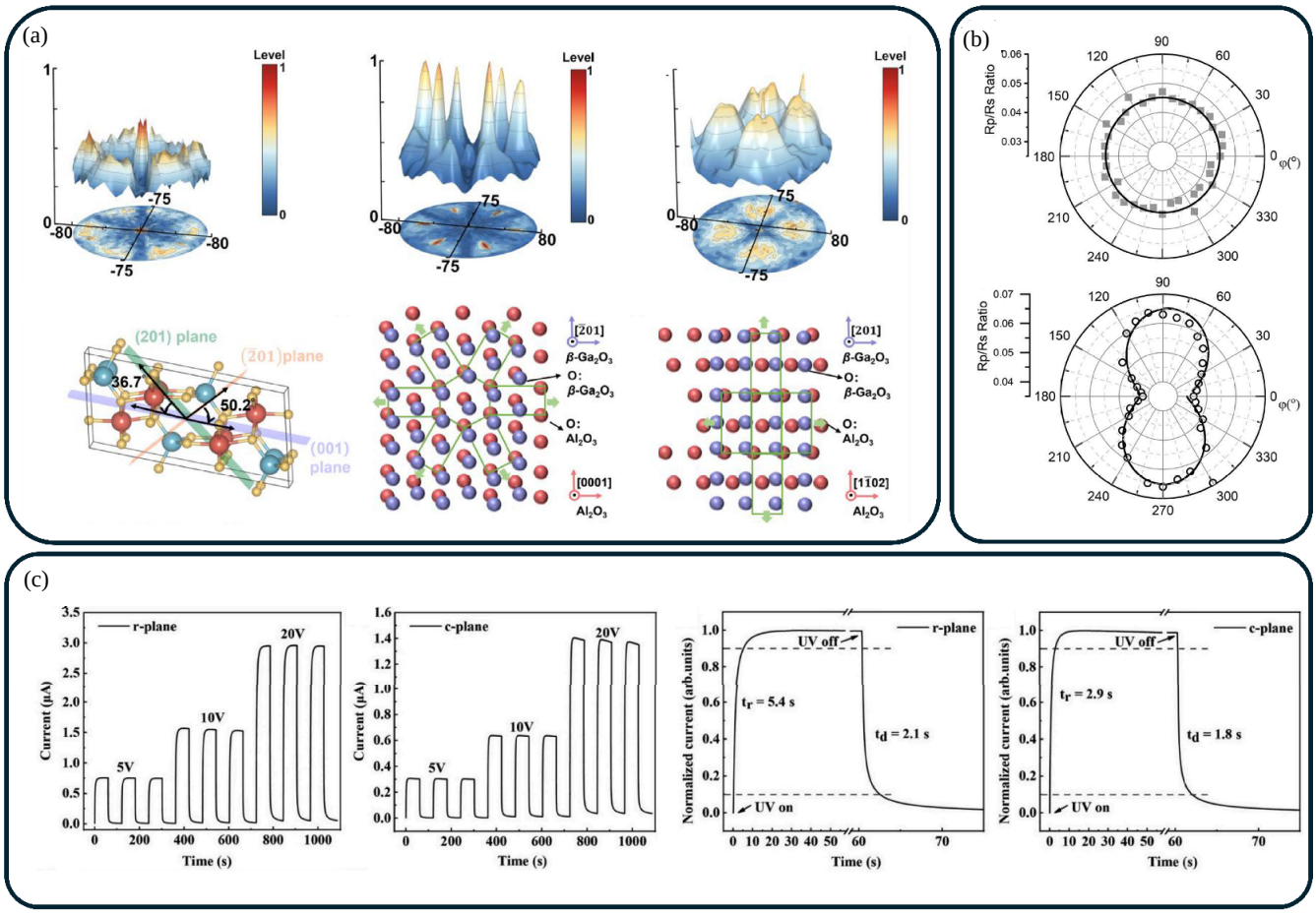

FIGURE 4. Substrate-controlled crystallographic orientation, optical anisotropy, and photoresponse of heteroepitaxial β-Ga_2O_3 films. (a) Pole figures, interplanar-angle geometry, and interfacial atomic arrangements of β-Ga_2O_3 films grown on c-plane and r-plane sapphire, illustrating the substrate-dependent rotational-domain configurations [35]. *Reproduced with permission under the terms of the Creative Commons CC BY 4.0 license*. (b) R_p/R_s polar plots at 210 nm for β-Ga_2O_3 films on c-cut and r-cut sapphire, showing nearly isotropic and pronounced two-lobed optical responses, respectively [59]. *Reproduced with permission under the terms of the Creative Commons CC BY 4.0 license*. (c) Time-dependent photoresponses of β-Ga_2O_3 photodetectors grown on r-plane and c-plane sapphire, revealing the slower response dynamics of the mixed-orientation r-plane film [61]. *Copyright 2020, Elsevier*. Together, these results demonstrate that substrate engineering simultaneously regulates domain orientation, macroscopic optical anisotropy, and defect-limited carrier dynamics.

tive. Ho et al. [59] independently observed the similar macroscopic contrast in pulsed laser deposition (PLD)-grown films: the R_p/R_s polar plot at 210 nm is nearly circular for the c-cut sample but exhibits a distinct two-lobed pattern for the r-cut sample (Fig. 4(b)). Their structural analysis further associated the r-cut anisotropy with tilted β-Ga_2O_3 grain orientations relative to the sapphire surface, indicating that substrate-controlled anisotropy can arise through growth-dependent epitaxial configurations rather than a single universal domain arrangement.

Substrate choice also influences anisotropy through direction-dependent lattice mismatch and defect formation. Ma et al. [60] compared $(\bar{2}01)$-oriented β-Ga_2O_3 films grown on c-plane GaN and sapphire. Although both heteroepitaxial films exhibited six-fold rotational domains, the rocking-curve broadening on GaN showed a clear six-fold anisotropy, with maxima along [010] and minima along [102], whereas that on sapphire was nearly isotropic. This difference was attributed primarily to the stronger directional contrast in lattice mismatch for GaN (4.67% along [010] and approximately 0% along [102]) than for sapphire (1.62% and -3.12%, respectively), resulting in different strain-relaxation and defect distributions. At the device level, Liu et al. [61] reported that β-Ga_2O_3 films grown on r-plane sapphire, containing mixed (100)- and (001)-oriented grains, achieved a responsivity of $\sim$170 A/W and a detectivity of 1.3×10^{14} Jones, compared with $\sim$91.9 A/W and 7.2×10^{13} Jones for the $(\bar{2}01)$-oriented films on c-plane sapphire. However, the mixed-orientation films exhibited a slower photoresponse (Fig. 4(c)), which was attributed to additional trapping and recombination centers introduced by the associated grain boundaries. These results reveal a substrate-engineering trade-off between enhanced photoresponse and defect-limited response speed. Overall, substrate engineering should therefore be regarded not simply as a means of maximizing polarization anisotropy, but as a strategy for balancing orientation and domain control against mismatch-induced defects and carrier-response dynamics.

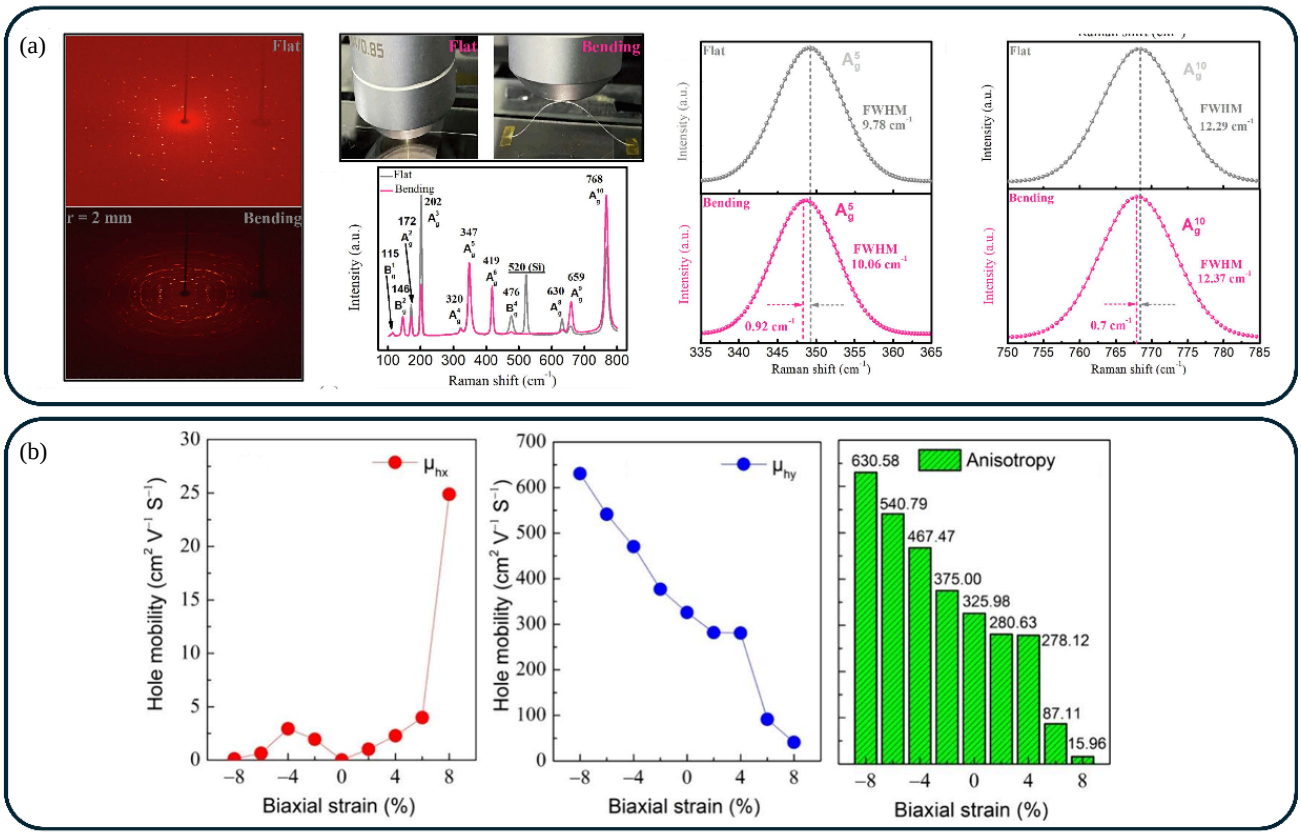

FIGURE 5. Strain-induced lattice distortion and carrier-transport modulation in β-Ga_2O_3. (a) XRD patterns, optical images, Raman spectra, and enlarged Raman peaks of flexible β-Ga_2O_3 (100) single-crystal microstrips in the flat and bending states, showing bending-induced lattice distortion and modified lattice vibration [62]. *Copyright 2022, Elsevier*. (b) Calculated strain-dependent hole mobilities along the x- and y-directions and the corresponding mobility anisotropy of Mg-doped 2D β-Ga_2O_3 [65]. *Copyright 2025, American Chemical Society*. In the original panel (b), mobility anisotropy is expressed as μ_y-μ_x, whereas μ_y/μ_x is adopted throughout this review for consistent cross-study comparison.

3.2. Strain Engineering

Mechanical strain provides an external means of tuning the anisotropic properties of β-Ga_2O_3 by perturbing its lattice structure and consequently modifying its optical and carrier-transport responses. Experiments on β-Ga_2O_3 single-crystal flakes show that compressive and tensile strains can affect polarization-dependent absorption differently, with compressive strain producing a stronger enhancement of the absorption anisotropy near the solar-blind detection wavelength [63]. In low-dimensional doped β-Ga_2O_3, first-principles calculations further show that strain modifies the band structure, deformation potentials, effective masses, and consequently the anisotropic carrier mobility [64, 65]. Thus, strain engineering can influence polarization-related performance through two distinct channels: modulation of anisotropic optical absorption and modification of direction-dependent carrier transport.

A direct demonstration of strain-modulated polarization sensitivity was reported by Zhang et al. [63] using a mechanically exfoliated β-Ga_2O_3 single-crystal flake. Under 0.7% compressive strain, the photocurrent under $E\perp b$ increased by a factor of 2.50 relative to the flat state, whereas that under $E//b$ increased by only 1.34, increasing the polarization ratio from 49 to 100. In contrast, 0.7% tensile strain enhanced the photocurrent by similar proportions for the two orthogonal polarizations and produced little change in the polarization ratio. DFT calculations attributed this asymmetric response to the substantially increased absorption-coefficient ratio α_c/α_b near 254 nm under compressive strain.

The influence of bending-induced strain on device response was further investigated by Yan et al. [62] using flexible β-Ga_2O_3 (100) single-crystal microstrips. Upon bending, the XRD pattern evolved from sharp single-crystal diffraction spots into a diffraction ring, while the Raman peaks exhibited changes in intensity, redshift, and broadening, confirming bending-induced lattice distortion and modified lattice vibration (Fig. 5(a)). As the bending radius decreased, both the photocurrent and dark current increased, with the largest variation observed for the device channel aligned with the bending direction. The enhanced photocurrent was associated with strain-modified photoabsorption and carrier generation, whereas the increased dark current and slower response were mainly related to bending-induced defects.

First-principles calculations further demonstrate that strain can strongly reshape anisotropic carrier transport in doped two-dimensional β-Ga_2O_3. For Ca-doped 2D β-Ga_2O_3, Zeng et al. [64] found that the hole mobility along the y-direction increased from 246.62 $cm^2V^{-1}s^{-1}$ in the unstrained state to 568.48 $cm^2V^{-1}s^{-1}$ under 4% tensile strain. Using the consistent mobility-ratio definition adopted in this review,

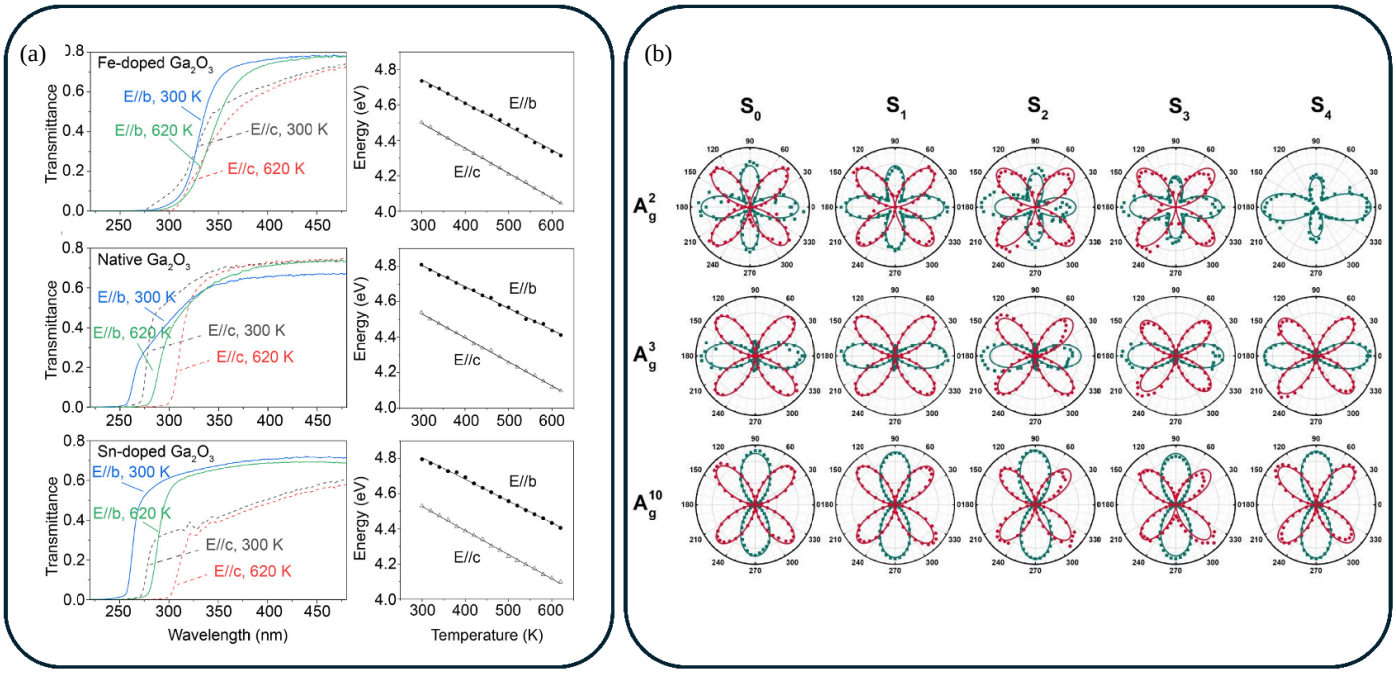

FIGURE 6. Doping- and alloying-modulated anisotropic optical and vibrational responses of β-Ga_2O_3. (a) Polarized transmission spectra at 300 and 620 K and temperature-dependent bandgaps of Sn-doped, unintentionally doped, and Fe-doped β-Ga_2O_3 for $E//b$ and $E//c$, showing the direction-dependent band-edge response and electron-phonon coupling [68]. *Copyright 2022, AIP Publishing*. (b) Angle-resolved polarized Raman polar plots of the A_g^2, A_g^3, and A_g^{10} modes in β-$(Al_xGa_{1-x})_2O_3$, illustrating the mode-dependent evolution of vibrational anisotropy with Al alloying [69]. *Reproduced with permission under the terms of the Creative Commons CC BY 4.0 license*. Together, these results show that chemical modification can selectively reshape different forms of anisotropy rather than uniformly enhancing the overall anisotropic response.

μ_y/μ_x decreases from approximately 1.23×10^4 to 2.15×10^2, indicating that enhancement of the absolute mobility does not necessarily preserve strong transport anisotropy. In Mg-doped 2D β-Ga_2O_3, compressive strain instead strongly favors y-direction transport, with μ_y reaching 630.69 $cm^2V^{-1}s^{-1}$ under -8% strain while the direct-bandgap character is retained (Fig. 5(b)) [65]. These results illustrate that the magnitude and anisotropy of carrier mobility can respond differently to strain, depending on the dopant and strain state. Overall, strain engineering provides a versatile route for tuning both optical absorption anisotropy and direction-dependent carrier transport in β-Ga_2O_3, although enhancement of one anisotropic property does not necessarily lead to simultaneous improvement of the others.

3.3. Doping and Alloying

Doping and alloying can modify the anisotropic response of β-Ga_2O_3 through several physically distinct pathways rather than through a single universal mechanism. Dopant incorporation can alter carrier scattering and localization, free-carrier concentration and dielectric screening, as well as electronphonon and excitonic interactions, whereas alloying additionally perturbs the lattice and vibrational anisotropy. These effects may enhance, suppress, or redistribute different forms of anisotropy depending on the dopant species, carrier concentration, crystallographic direction, and alloy composition. The following discussion therefore distinguishes transport-related effects from optical/excitonic modulation and alloy-induced lattice responses.

Dopant incorporation can also interact with the pre-existing crystallographic anisotropy, as illustrated by the distinct Raman responses and etch-pit morphologies observed on the (100) and (001) surfaces of V-doped β-Ga_2O_3 [66]. More directly, doping can substantially reshape direction-dependent carrier transport. Wang et al. [57] found that unintentionally doped quasi-2D β-Ga_2O_3 exhibits only weak in-plane mobility anisotropy ($\mu_{max}/\mu_{min} \approx 1.4$), whereas Si-doped flakes show a conductivity ratio of approximately 5.7 and a photoresponsivity ratio of 5.1 between the c- and b-axis directions. The authors associated this enhanced anisotropy with extrinsic effects related to doping and carrier localization, while noting that its microscopic origin remains unresolved. Consistently, THz measurements by Wang et al. [67] revealed qualitatively different carrier dynamics along the a- and c-axes of (010) β-Ga_2O_3: the a-axis response follows a Drude model, whereas the c-axis requires a Drude-Smith description, indicating much stronger carrier localization along c. In Fe-doped crystals, the a-axis mobility is further enhanced by the low carrier density and reduced phonon scattering.

Doping also modifies the anisotropic optical response by changing free-carrier populations and the associated screening and scattering environment. Cheng et al. [68] compared Sn-doped, unintentionally doped, and Fe-doped β-Ga_2O_3 and found that the temperature-induced bandgap reduction is consistently larger for $E//c$ than for $E//b$ (Fig. 6(a)). The extracted electronphonon coupling parameter β follows the

same directional trend for all three samples, with values of 1.37/1.23, 1.36/1.22, and 1.41/1.33 meVK^{-1} for $E//c/E//b$ in the Sn-doped, unintentionally doped, and Fe-doped crystals, respectively. Because the larger β for $E//c$ produces a stronger temperature-dependent band-edge renormalization than for $E//b$, the relative absorption coefficients for the two polarizations can vary near the absorption edge. However, Ref. [68] does not provide polarization-resolved device measurements that establish a corresponding change in photocurrent *PR*, and the electronphonon result should therefore be interpreted as an optical-anisotropy mechanism rather than direct evidence of device-level PR tuning. This comparison indicates that the crystallographic anisotropy of electronphonon coupling is retained across different doping conditions, while the dopant-dependent changes in its magnitude are comparatively modest. In contrast, the excitonic response is strongly influenced by carrier screening: exciton-polariton features are most evident in the semi-insulating Fe-doped crystal, become weaker in the unintentionally doped sample, and are not visibly resolved in the highly conductive Sn-doped crystal because increased free-carrier screening suppresses effective exciton formation. Polarized photoluminescence measurements further show that doping can modify direction-selective radiative recombination without producing a universal enhancement of optical anisotropy. Cooke et al. [70] found that unintentionally doped and Sn-doped β-Ga_2O_3 retain similar polarized emission characteristics, with emission generally strongest along c (or c^*) and weakest along b, while Sn incorporation primarily quenches the overall PL intensity rather than fundamentally changing the emission spectrum. Fe-doped crystals exhibit qualitatively different behavior because Fe-induced semi-insulating conditions enable red emission from unintentionally incorporated Cr^{3+} centers, leading to polarization characteristics distinct from those of the band- and defect-related UV/blue emission. These results demonstrate that dopant effects on optical anisotropy depend on whether the relevant process is band-edge absorption, carrier screening, or defect-mediated radiative recombination.

In the area of alloying modulation, Li et al. [69] employed a spatial correlation model and angle-resolved polarized Raman spectroscopy to systematically study the anisotropy of β-$(Al_xGa_{1-x})_2O_3$ single crystals with x up to 0.26. With increasing Al content, the Raman tensor anisotropy of the low-frequency A_g^2 and A_g^3 modes is enhanced, whereas that of the high-frequency A_g^{10} mode is weakened, demonstrating a mode-dependent redistribution rather than a uniform enhancement of vibrational anisotropy (Fig. 6(b)). The contrasting trends were associated with the different lattice-vibration characteristics and bond-polarizability responses of the low- and high-frequency phonon modes. Thus, alloying should be regarded as a means of selectively reshaping specific anisotropic lattice responses rather than simply increasing the overall anisotropy of β-Ga_2O_3. Overall, doping and alloying should be viewed as mechanism-selective tuning strategies rather than universal anisotropy enhancers, because carrier transport, excitonic screening, radiative recombination, and lattice-vibrational anisotropy need not evolve in the same direction.

3.4. Structural Engineering

Structural engineering can modify the polarization response of β-Ga_2O_3 through mechanisms that should be distinguished from its intrinsic crystallographic anisotropy. In single-crystalline β-Ga_2O_3 nanostructures, the monoclinic-lattice dichroism can be retained while the device geometry introduces additional polarization-dependent field confinement or morphology-related effects [72]. Periodic patterning of the β-Ga_2O_3 active layer can further reshape both optical absorption and interfacial band structure [71]. By contrast, external subwavelength metal gratings introduce polarization selectivity through anisotropic electromagnetic boundary conditions and resonant transmission, and can therefore generate polarization sensitivity even when the underlying semiconductor is isotropic [73, 74]. When such gratings are coupled to an anisotropic dielectric, the resulting resonances can additionally depend on specific components of the dielectric tensor [75]. Accordingly, the following discussion separates crystal-anisotropy-assisted β-Ga_2O_3 nanostructures from externally imposed grating-based polarization filtering.

As a representative case in which crystallographic anisotropy remains the dominant mechanism, Chen et al. [72] reported a solar-blind ultraviolet polarization-sensitive photodetector based on CVD-grown β-Ga_2O_3 nanobelts. DFT calculations revealed that the polarization-dependent optical transitions produce substantially different absorption along the two principal nanobelt directions. The calculated absorption coefficient at 254 nm along the [202] direction is ~6.5 times larger than that along the [020] direction, reflecting the strong intrinsic dichroism of monoclinic β-Ga_2O_3. The long and short axes of the nanobelt correspond to the [202] and [020] directions, respectively. The metal-semiconductor-metal (MSM) photodetector fabricated from these nanobelts exhibited pronounced polarization-dependent photocurrent and response dynamics under 254 nm illumination (Fig. 7(b)). Using the I_{max}/I_{min} definition adopted in this review, its reported anisotropy parameter corresponds to a polarization ratio of approximately 49. Importantly, FDTD simulations yielded only a small morphology-induced anisotropy (~0.13), indicating that the polarization response is dominated by intrinsic dichroism rather than by the one-dimensional geometry, although both mechanisms can contribute.

Beyond simply retaining the intrinsic dichroism, periodic patterning of the β-Ga_2O_3 active layer can actively reshape both its optical and electrical response. Wang et al. [71] reported a solar-blind photodetector based on a β-Ga_2O_3 nanograting structure that combines photonic and band engineering. Technology computer-aided design (TCAD) analysis attributed the suppressed dark current to nanograting-induced surface-state-related band bending and strengthened depletion at the Ti/β-Ga_2O_3 interface, whereas optical simulations and measurements showed enhanced absorption arising from reduced reflection and transmission, light trapping, and intensified local fields (Fig. 7(a)). The optimized NG-P300 device achieves a responsivity of 174.8 A/W and a specific detectivity of 1.7×10^{14} Jones, while reducing the dark current to 1.8×10^{-14} A. Using I_{max}/I_{min} consistently, the polarization

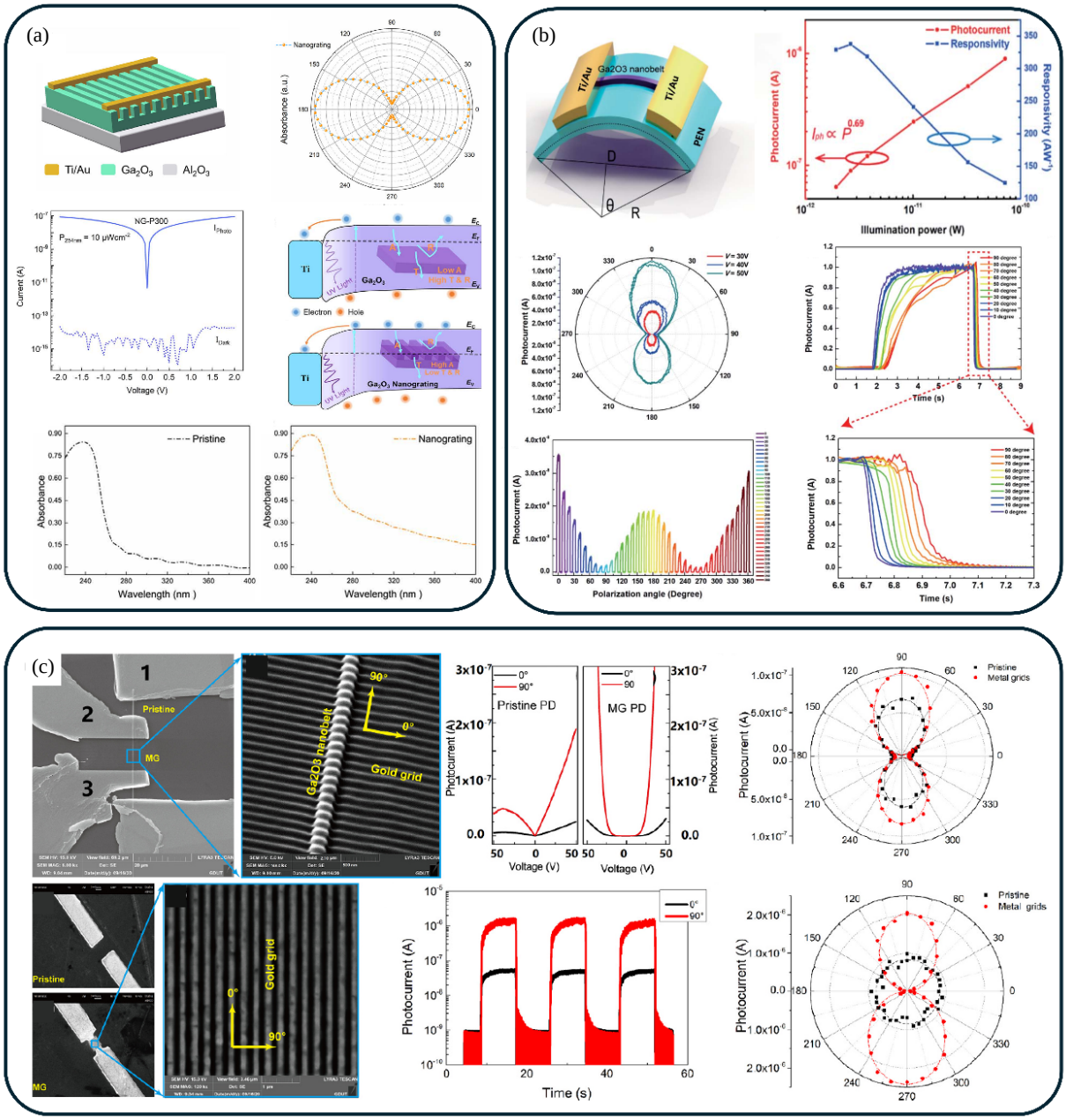

FIGURE 7. Structural modulation of polarization-sensitive β-Ga_2O_3 photodetectors. (a) β-Ga_2O_3 nanograting device architecture, polarization-dependent simulated absorbance, electrical characteristics, interfacial band modulation, and experimental UV absorption, illustrating the coupled optical and electronic effects introduced by periodic patterning [71]. *Reproduced with permission under the terms of the Creative Commons CC BY 4.0 license*. (b) Flexible single-crystalline β-Ga_2O_3 nanobelt photodetector and its power-, polarization-, and time-dependent photoresponse, demonstrating polarization discrimination dominated by intrinsic crystallographic dichroism [72]. *Reproduced with permission under the terms of the Creative Commons CC BY 4.0 license*. (c) β-Ga_2O_3 nanobelt and ZnO photodetectors with and without subwavelength metal grids, showing that externally imposed grating anisotropy can both enhance an intrinsically anisotropic β-Ga_2O_3 response and generate polarization sensitivity in an initially isotropic ZnO device [74]. *Copyright 2021, Elsevier*. Together, these results illustrate that structural engineering can preserve, reshape, amplify, or create polarization selectivity through physically distinct mechanisms.

ratio increases from approximately 1.4 for the planar device to 5.7 after nanograting patterning. Thus, unlike the nanobelt case in which intrinsic dichroism dominates, the nanograting response reflects the coupled influence of the β-Ga_2O_3 material anisotropy, geometry-induced optical anisotropy, and interfacial band modulation.

Beyond patterning the β-Ga_2O_3 active layer itself, external subwavelength metal gratings can impose an additional polarization-selective optical response that is independent of crystallographic dichroism. Zhang et al. [73] integrated subwavelength gold gratings with amorphous Ga_2O_3 thin films to construct a deep-ultraviolet polarization detector. Although amorphous Ga_2O_3 is intrinsically isotropic, the grating produces strongly polarization-dependent transmission: according to effective medium theory (EMT) and finite-difference time-domain (FDTD) calculations, the component polarized parallel

to the grating lines (0°) is predominantly reflected, whereas the orthogonal component (90°) is preferentially transmitted. Under 254 nm illumination, an extinction ratio as high as 21.49 is achieved between 90° and 0° polarized light, and FDTD simulations further confirm that the transmittance of the former is approximately 2.22 times that of the latter. This result provides a clear control case showing that structural anisotropy alone can generate polarization sensitivity in an otherwise isotropic active material. Zhang et al. [74] further combined this extrinsic filtering mechanism with the intrinsic anisotropy of single-crystalline β-Ga_2O_3 nanobelts by integrating subwavelength metal gratings with β-Ga_2O_3 nanobelts and ZnO thin films. For β-Ga_2O_3 nanobelts, the polarization ratio of the pristine device is 7.5, which is increased to 49 after grating integration; for the originally isotropic ZnO thin film, a polarization ratio of 26 is also obtained after grating integration (Fig. 7(c)). FDTD simulations indicate that the metal grids preferentially attenuate the polarization component parallel to the ridges while facilitating transmission of the orthogonal component through surface plasmon polariton (SPP)-associated field coupling. Thus, Ref. [73] demonstrates polarization selectivity created entirely by an artificial grating, whereas Ref. [74] shows that the same structural mechanism can be superimposed on intrinsic β-Ga_2O_3 dichroism to further amplify the device-level polarization contrast.

From a different perspective, Jia et al. [75] examined the THz response of metallic gratings on anisotropic dielectric substrates and showed that the narrow $TM_{1,1}$ waveguide resonance is governed mainly by the grating period and the out-of-plane refractive index, while substrate thickness and in-plane refractive indices have little influence on its spectral position in electromagnetically thick substrates. Although this study was developed for refractive-index characterization rather than photodetection, it demonstrates that grating resonances coupled to anisotropic β-Ga_2O_3 can selectively probe specific components of the dielectric tensor. Thus, intrinsic dielectric anisotropy and structure-induced electromagnetic resonances should not always be treated as independent contributions. Overall, structural engineering can preserve, reshape, amplify, or even create polarization selectivity, but the operative structural contribution must be distinguished from intrinsic crystallographic anisotropy when interpreting and comparing device-level polarization performance.

4. DEVICE-LEVEL PERFORMANCE AND SYSTEM INTEGRATION

Having established the microscopic origins and external modulation of anisotropy, the next question is how effectively these properties are translated into measurable device performance and, ultimately, usable polarization information. Device-level polarization performance cannot be assessed by a single figure of merit: responsivity and detectivity describe signal sensitivity, polarization ratio quantifies discrimination between polarization states, and temporal response determines the usable bandwidth, while operating bias, illumination conditions, device geometry, and gain mechanisms strongly affect their comparability across studies. This section therefore moves from single-device benchmarking to interface-assisted self-powered operation and finally to polarimetric reconstruction and imaging, with emphasis on the trade-offs and information-transfer capability rather than on record values alone.

4.1. Performance Metrics, Benchmarking, and Trade-offs

Meaningful benchmarking of β-Ga_2O_3 polarization-sensitive photodetectors requires consideration of multiple performance dimensions rather than any single record value. Responsivity and detectivity describe signal sensitivity, polarization ratio quantifies discrimination between polarization states, and temporal response determines how rapidly polarization information can be read out. However, these metrics are not independent and are strongly influenced by operating bias, illumination conditions, device geometry, carrier-gain mechanisms, and noise assumptions. Consequently, a device exhibiting an exceptionally high polarization ratio or responsivity does not necessarily provide the best overall polarization-detection performance. To establish a consistent basis for the cross-study comparison that follows, the principal device figures of merit and the definitions adopted in this review are first summarized below.

Accordingly, the principal figures of merit considered in this review include Responsivity (R), Detectivity (D^*), Polarization ratio (PR), and response speed. Their definitions and corresponding formulas are summarized as follows:

Responsivity (R): Defined as the ratio of the output photocurrent (I_{photo}) to the incident optical power (P_{inc}), characterizing the efficiency of the device in converting optical signals into electrical signals, expressed in A/W [76–78]:

$$R = \frac{I_{photo}}{P_{inc}} \tag{2}$$

External Quantum Efficiency (EQE): Defined as the ratio of the number of photogenerated carriers collected per unit time to the number of incident photons, reflecting the photon utilization efficiency of the device [79–81]:

$$EQE = \frac{Rhc}{q\lambda} \times 100\% \tag{3}$$

where q is the elementary charge, h is Planck's constant, c is the speed of light, and λ is the wavelength of the incident light.

Detectivity (D^*): The normalized detectivity quantifies the ability of a detector to resolve weak signals from noise, with units of Jones ($cm \cdot Hz^{1/2} \cdot W^{-1}$). When dark current shot noise is the dominant noise source, D^* can be simplified as [82–84]:

$$D^* = \frac{R\sqrt{S}}{\sqrt{2qI_{dark}}} \tag{4}$$

where S is the effective device area and I_{dark} is the dark current.

Polarization Ratio (PR): Defined as the ratio of the I_{photo} (or R) under orthogonal polarization directions, used to quantify the polarization sensitivity of the device [85–87]:

$$PR = \frac{I_{\max}}{I_{\min}} \tag{5}$$

TABLE 3. Representative device-level performance metrics of β-Ga_2O_3 polarization-sensitive photodetectors with different material forms, device structures, and crystallographic orientations. (All measurements listed in Table 3 were performed at 254 nm; the only exception is the 2D flake device [99], which was characterized at 265 nm.)

Material morphology	Crystallographic plane	Polarization ratio (PR)	R (A/W)	D^* (Jones)	τ_r/τ_d (ms)	Bias (V)	Ref.
Single crystal (bulk)	(100)	∼1.8	–	–	–	–	[95]
Single crystal (bulk)	(010)	1.2	1.1	3.08×10^{12}	∼2/2	0	[91]
Single crystal (bulk)	(001)	5.8	–	–	–	0	[91]
Nanoribbon	(100)	$>$ 3000 (max 5276)	10.25	–	–	10	[90]
Nanobelt	along [202]	49	335	–	–	17	[72]
Nanograting	(201)	5.7	174.8	1.7×10^{14}	0.52/0.62	–	[71]
Microwire	(100)	137	–	–	-/90	–	[96]
Thin film	(201)	6.02	–	–	20/1210	–	[35]
Thin film	$(\bar{2}01)$	1.63	–	–	–	–	[97]
Thin film	$(\bar{1}02)$	∼1.1	114.4	4.55×10^{15}	107.3/99.4	5	[98]
2D flake	(100)	∼2.8	–	–	0.1/0.078	2	[99]
Nanobelt + metal grating	along [202]	49	–	–	–	–	[74]

where I_{max} and I_{min} are the maximum and minimum photocurrent values in a polarization angle scan, respectively. Some studies also adopt the polarization extinction ratio ($ER = 10\log_{10}(I_{max}/I_{min})$) or the normalized photocurrent difference ratio ($\sigma = (I_{max} - I_{min})/(I_{max} + I_{min})$) as alternative figures of merit. Throughout this review, "polarization ratio" refers to I_{max}/I_{min} unless otherwise noted. The term "dichroic ratio" is reserved for absorption coefficient anisotropy, distinguishing it from photocurrent-based metrics.

Response Time (τ_r and τ_d): Defined as the time required for the photocurrent to rise from 10% to 90% of its steady-state value (rise time, τ_r) and to decay from 90% to 10% of its steady-state value (decay time, τ_d), reflecting the response speed of the device [88, 89].

Representative β-Ga_2O_3 polarization photodetectors occupy markedly different performance regimes rather than following a single trajectory toward simultaneously higher values of all figures of merit. At the high-contrast end, Zhao et al. [90] reported CVD-grown β-Ga_2O_3 nanoribbon detectors with $PR > 3000$ over most tested biases and a peak value of 5276 at 10 V under 254 nm illumination (5 $mWcm^{-2}$), together with a responsivity of 10.25 A/W. However, approximately 1 min of illumination was allowed for the detector to establish its response along each polarization direction, indicating that this exceptionally large *PR* primarily characterizes steady-state polarization discrimination rather than high-speed readout. Mechanically exfoliated β-Ga_2O_3 microwires provide another high-contrast regime, reaching a *PR* of 137 at 254 nm while showing good device reproducibility [96]. By contrast, ultrathin 2D β-Ga_2O_3 flakes exhibit a more modest *PR* of approximately 2.8, but achieve much faster rise/decay times of 100/78 µs and stable polarization-dependent response over repeated switching cycles [99]. These results illustrate that maximizing polarization contrast and maximizing temporal response are distinct device-design objectives, and that a lower *PR* does not necessarily imply inferior functionality when rapid polarization readout is required.

A similar decoupling is evident among sensitivity, spectral selectivity, and polarization discrimination. Nanograting engineering can substantially enhance electrical sensitivity, as the optimized β-Ga_2O_3 nanograting detector reaches $R = 174.8$ A/W and $D^* = 1.7 \times 10^{14}$ Jones while providing a *PR* of 5.7 [71]. Conversely, the $(\bar{1}02)$-oriented β-Ga_2O_3 thin-film detector reported by Gu et al. [98] achieves $R = 114.4$ A/W and a reported $D^* = 4.55 \times 10^{15}$ Jones at 5 V, but its polarization ratio is only approximately 1.1, demonstrating that high photosensitivity does not necessarily translate into strong polarization discrimination. Chen et al. [93] targeted yet another performance dimension by exploiting the polarization-dependent absorption edge of (100) β-Ga_2O_3 together with an orthogonally aligned crystal filter, achieving narrow-band detection centered near 262 nm with a bandwidth of approximately 10 nm, a UVC/UVA rejection ratio above 800, and a total response time of 0.86 ms. Dong et al. [94] used a back-illumination architecture to avoid electrode shadowing and obtained a fast general UV transient response of 24 µs/1.24 ms, while polarization sensitivity was demonstrated separately. Collectively, these studies show that *PR*, responsivity, detectivity, spectral selectivity, and response speed should be regarded as complementary rather than interchangeable performance dimensions. Table 3 therefore serves as a multidimensional benchmark rather than a ranking based on any single record value.

Taken together, Table 3 shows that no single device architecture simultaneously maximizes polarization contrast, photosensitivity, response speed, and low-bias operation. Device optimization should therefore target a performance balance matched to the intended polarization-information task rather than a record value in any individual metric.

4.2. Interface Engineering for Self-powered Polarization Detection

For polarization-sensitive β-Ga_2O_3 photodetectors, interface engineering is important not because a heterojunction necessar-

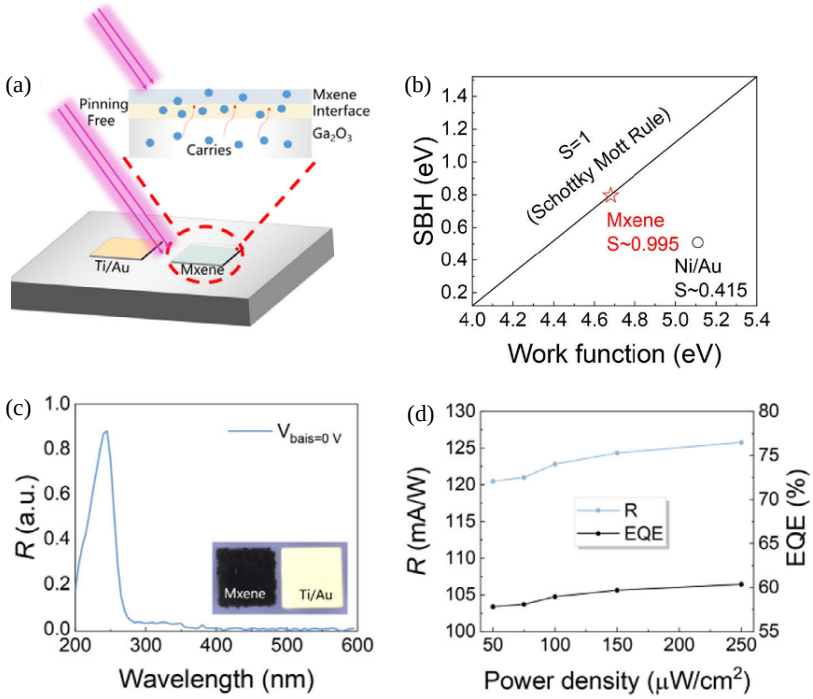

FIGURE 8. Interface and photoresponse characteristics of the $Ti_3C_2T_x/\beta$-Ga_2O_3 van der Waals Schottky photodiode. (a) Device schematic. (b) Extracted Schottky barrier height as a function of metal work function. (c) Spectral photoresponse, with an image of the complete device shown in the inset. (d) The *R* and *EQE* under self-powered operation [92]. *Reproduced with permission under the terms of the Creative Commons CC BY 4.0 license*.

ily creates polarization selectivity, but because interfacial energetics and built-in electric fields determine how polarization-dependent photocarriers are separated and collected without an external bias. In this review, self-powered operation refers to a reproducible photoresponse at zero applied bias driven by an internal electric field. The relevant interface therefore needs to be evaluated from two coupled perspectives: its ability to suppress recombination and facilitate carrier extraction, and its influence on the preservation or modification of the intrinsic anisotropic photoresponse of β-Ga_2O_3. Accordingly, this subsection focuses primarily on interfaces that directly enable or clarify self-powered polarization detection, while broader β-Ga_2O_3 heterojunction studies are considered only when they provide transferable insight into interface quality, band alignment, or carrier-separation mechanisms.

A zero-bias photoresponse alone is not sufficient to establish genuine photovoltaic self-powered operation. Its physical origin should be distinguished from asymmetric photoconduction, persistent photoconductivity, pyroelectric contributions, and contact-related artifacts by examining the spatial origin, polarity, and reproducibility of the zero-bias signal. Depending on the device architecture, complementary measurements such as photocurrent mapping, capacitance-voltage or capacitance-frequency analysis, and spectroscopic determination of work functions or band offsets can provide evidence for the depletion region, interface states, and interfacial energetics underlying the proposed built-in field. Accordingly, band-alignment diagrams in this review are treated as mechanistic models that require experimental support rather than as independent proof of the charge-transfer direction.

An important prerequisite for interface-assisted polarization detection is that the heterointerface itself can depend strongly on β-Ga_2O_3 crystal orientation. Mudiyanselage et al. [100] compared NiO_x/β-Ga_2O_3 *pn* heterojunctions formed on $(\bar{2}01)$, (001), and (010) substrates and observed pronounced orientation-dependent electrical behavior. Capacitance-frequency analysis yielded interface trap densities of 4.3×10^{10}, 7.4×10^{10}, and $1.6\times10^{11}\ eV^{-1}\ cm^{-2}$ for the $(\bar{2}01)$, (001), and (010) interfaces, respectively. These results demonstrate a clear crystallographic-orientation dependence of the interfacial electronic properties. However, the higher interface trap density of the (010) junction should not be attributed directly to its lower surface dangling-bond density, because surface dangling bonds and electrically active interface traps are physically distinct quantities and the reported data do not establish a simple monotonic relationship between them. The microscopic origin of the orientation dependence should therefore be interpreted more cautiously as involving the overall surface and interface configuration rather than a single surface parameter. These results show that crystal orientation affects not only the intrinsic anisotropic properties of β-Ga_2O_3 but also the quality and carrier dynamics of a subsequently formed heterointerface. Ref. [100], however, addresses the anisotropic electrical properties of the junction rather than polarization-resolved photodetection, and its relevance here is therefore mechanistic rather than evidence of direct polarization enhancement.

Direct self-powered polarization detection can be realized through asymmetric Schottky contacts without introducing a semiconductor *pn* heterojunction. Long et al. [91] fabricated β-Ga_2O_3 Schottky photodiodes using Ti/Au and Pt/Ti/Au con-

tacts, with the former forming an Ohmic contact and the latter providing the Schottky barrier. Photocurrent mapping at zero bias localized the photoresponse near the Pt Schottky junction, supporting the built-in-field origin of the photovoltaic response. The device performance was strongly orientation dependent: the (010) photodiode exhibited a responsivity of 1.1 A/W and a detectivity of 3.08×10^{12} Jones at zero bias, whereas the polarization ratio increased from approximately 1.2 for the (010) orientation to 5.8 for the (001) orientation. This comparison shows that the Schottky junction provides the zero-bias carrier-collection mechanism, while the magnitude of polarization discrimination remains governed primarily by the crystallographic orientation of β-Ga_2O_3. Interface engineering can further improve this conversion from anisotropic photogeneration to zero-bias electrical readout. Li et al. [92] replaced a conventional metal contact with a $Ti_3C_2T_x/\beta$-Ga_2O_3 van der Waals Schottky interface (Fig. 8). The vdW contact exhibited an interface-state density approximately one order of magnitude lower than that of a conventional Ni/β-Ga_2O_3 contact and a Fermi-level-pinning factor of $S \approx 0.995$, approaching the Schottky-Mott limit. The resulting device showed a self-powered responsivity of 125.1 mA/W, rise/decay times of 0.27/0.29 ms, and a polarization ratio of 7.1 at zero bias. These results indicate that reducing interfacial trapping and Fermi-level pinning can improve carrier extraction while retaining the intrinsic polarization selectivity of β-Ga_2O_3; importantly, the vdW interface enhances the electrical readout of anisotropic photogeneration rather than constituting the primary microscopic origin of the polarization dependence.

A *p-n* heterointerface provides an alternative route to self-powered polarization readout, but its influence on polarization contrast need not be uniformly beneficial. Chen et al. [115] constructed a β-Ga_2O_3/PEDOT:PSS heterojunction using mechanically exfoliated β-Ga_2O_3 microwires. The resulting type-II band alignment produces interfacial band bending and a built-in electric field that separates photogenerated electrons and holes at zero bias, while PEDOT:PSS additionally serves as a hole-transport layer. The heterojunction retained a clear polarization-dependent response under self-powered operation, with $PR \approx 5$ and good device-to-device reproducibility, compared with a *PR* of 136 for the corresponding bare β-Ga_2O_3 microwire detector. This substantial reduction in polarization contrast is instructive: the heterointerface enables zero-bias carrier extraction but does not amplify the intrinsic anisotropy of β-Ga_2O_3. Rather, it preserves sufficient polarization information for self-powered readout, as further demonstrated by polarization-dependent ultraviolet image transmission. Thus, interface engineering should be evaluated not only by its ability to increase carrier-separation efficiency, but also by how much of the original polarization contrast survives the additional transport and recombination processes introduced at the heterointerface.

Beyond the polarization-sensitive devices discussed above, broader β-Ga_2O_3 heterojunction studies provide useful mechanistic guidance for interface design. For example, *p*-GaSe/*n*-Ga_2O_3 van der Waals heterojunctions employ type-II band alignment to facilitate photocarrier separation across a lattice-mismatch-tolerant interface [112], whereas MoS_2/β-Ga_2O_3 vdW heterostructures demonstrate that band alignment, electrode-interface barriers, and grain-boundary carrier populations can simultaneously influence responsivity, response speed, and dark current [113]. Organicinorganic integration offers another route: the C8-BTBT/β-Ga_2O_3 coreshell heterojunction combines type-II carrier separation with oxygen-vacancy control, where post-annealing suppresses defect-related dark current and improves weak-light detection [114]. These studies illustrate transferable strategies for controlling carrier separation, interfacial recombination, and defect-mediated transport. However, they primarily address general solar-blind ultraviolet photodetection rather than polarization-resolved operation. Therefore, they do not yet establish whether the engineered interfaces preserve, amplify, or partially obscure the intrinsic anisotropic response of β-Ga_2O_3 when incorporated into polarization-sensitive devices.

Surface chemistry and environmental stability are also important considerations for layered Ga-based chalcogenides because the chemically and electronically active interface may evolve substantially from its pristine state during processing or ambient exposure. Gutiérrez et al. [120] systematically compared nanometer-thick GaS, GaSe, and GaTe and found a progressive decrease in air stability from GaS to GaSe to GaTe; GaSe oxidation could be effectively suppressed by hydrogen passivation. Controlled oxidation can also be intentionally exploited for interface engineering. Cottam et al. [121] demonstrated that thermal oxidation of epitaxial GaSe proceeds through an intermediate Ga_2Se_3 phase and amorphous Ga_2O_3 before the formation of crystalline β-Ga_2O_3, illustrating how oxygen exposure can fundamentally alter the surface composition and resulting interfacial properties. Similarly, AlMutairi et al. [122] used O_2-plasma treatment to form an approximately 4 nm amorphous GaS_xO_y layer on GaS while largely preserving the underlying GaS lattice, thereby creating a controlled oxide/semiconductor heterostructure. These studies indicate that Ga-chalcogenide-based interfaces should be evaluated in terms of their actual chemically evolved interfaces rather than pristine-material band structures alone, because oxidation and passivation may influence band alignment, interface states, carrier separation, and long-term stability.

A comprehensive treatment of Ga_2O_3 heterojunction materials, fabrication routes, and general deep-ultraviolet photodetection performance is beyond the scope of this polarization-focused review and has been provided in recent dedicated reviews [118, 119]. Together with the layered Ga-based chalcogenide studies discussed above [116, 117, 120–122], these works show that heterojunction performance can depend jointly on interface quality, built-in-field carrier separation, defect control, surface chemistry, environmental stability, device geometry, and fabrication compatibility.

4.3. Polarimetric Reconstruction and Imaging Systems

Translating polarization-sensitive photocurrent into imaging requires more than a large device-level polarization ratio. A single anisotropic detector can distinguish selected polarization states, but quantitative polarimetry requires multiple in-

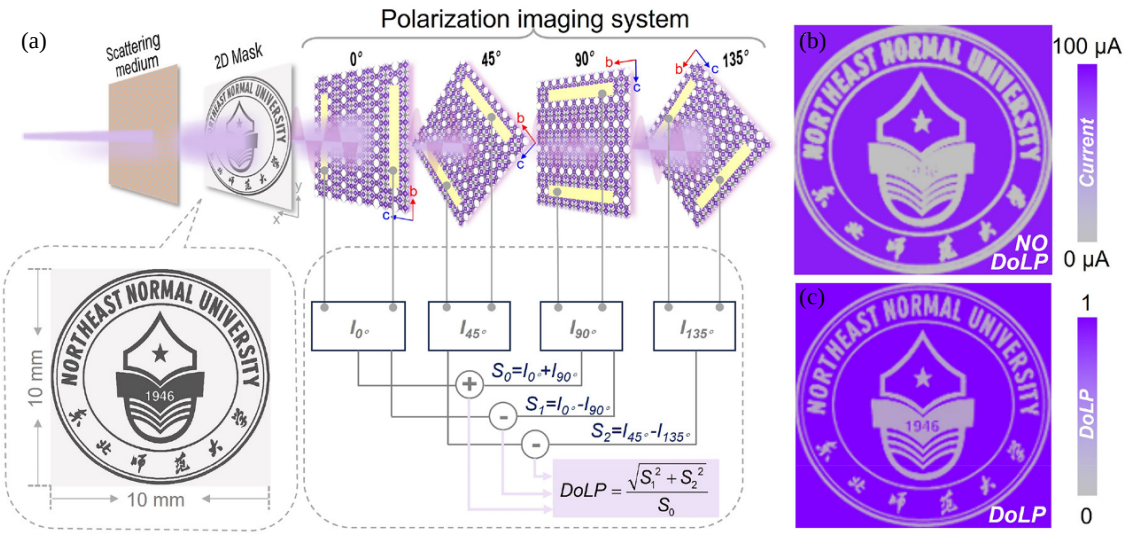

FIGURE 9. Single-pixel solar-blind ultraviolet polarization imaging based on twistedly stacked 2D β-Ga_2O_3 photodetectors. (a) System configuration employing four β-Ga_2O_3 detectors to simultaneously acquire polarization-dependent photocurrents at 0°, 45°, 90°, and 135° at each sampling position; a patterned school-badge mask and scattering medium are used for the imaging demonstration. (b) Direct photocurrent image obtained from the first β-Ga_2O_3 detector. (c) DoLP image reconstructed from the four polarization channels using the first three Stokes parameters, yielding a 150 × 150-pixel scanned image with improved structural contrast under scattering conditions [99]. *Copyright 2024, AIP Publishing*.

dependent response channels from which the incident polarization state can be reconstructed without ambiguity. For linearly polarized light, this generally involves resolving the first three Stokes parameters (S_0, S_1 and S_2), from which quantities such as the degree of linear polarization (DoLP) and polarization angle can be obtained. Existing β-Ga_2O_3 imaging demonstrations span different levels of information retrieval, ranging from polarization-dependent intensity contrast to quantitative polarization reconstruction. The following discussion therefore distinguishes polarization-contrast imaging from polarimetric imaging in which polarization information is explicitly reconstructed from multiple detector responses.

At the level of polarization-contrast imaging, detector arrays can spatially map polarization-dependent intensity without explicitly reconstructing the incident polarization state. Gu et al. [98] fabricated a 25-pixel ultraviolet photodetector array based on anisotropic $(\bar{1}02)$-oriented β-Ga_2O_3 films grown on MgO (110). Under 254 nm illumination, the $(\bar{1}02)$ device exhibited a characteristic two-lobed polarization-dependent photocurrent with $PR \approx 1.1$, whereas the $(\bar{2}1)$-oriented counterpart showed an approximately polarization-independent response. For imaging, a metallic mask patterned with the letter "N" was placed between the polarization-control optics and the detector array, and the spatial photocurrent distribution was recorded under 0° and 90° polarized illumination. The resulting 25-pixel maps exhibited distinguishable image contrast between the two polarization states. This experiment demonstrates array-level spatial readout of polarization-dependent intensity; however, because it compares predefined polarization states rather than reconstructing an unknown polarization state, it should be regarded as polarization-contrast imaging rather than quantitative polarimetric imaging.

A more complete information-reconstruction scheme was demonstrated by Zhong et al. [99] using ultrathin single-crystalline β-Ga_2O_3 flakes prepared by liquid-metal-assisted exfoliation. The exfoliated flakes were approximately 6 nm thick with lateral dimensions exceeding 5 mm, and the corresponding photodetectors exhibited a polarization ratio of approximately 2.8 and rise/decay times of 100/78 μs under 265 nm illumination. Rather than relying on the output of a single anisotropic detector, the authors constructed a three-channel vertically stacked polarimeter. Channel I consists of an optically isotropic amorphous Ga_2O_3 detector whose photocurrent varies approximately linearly with incident power, and is therefore calibrated as $I_I = aP + b$, where P is the incident optical power density and a and b are calibration coefficients. Channels II and III consist of two anisotropic 2D β-Ga_2O_3 flakes stacked with a relative rotation of 45°. Their polarization-dependent photocurrents can be represented by sinusoidal calibration functions with a 45° phase offset, $I_{II}(\theta) = A \cdot \sin^2(\theta + \varphi_{II})$, $I_{III}(\theta) = A \cdot \sin^2(\theta + 45° + \varphi_{III})$, where θ is the incident linear-polarization angle and the coefficients are determined experimentally. Because a single sinusoidal channel can correspond to two different polarization angles within a 180° period, simultaneous measurement of I_{II} and I_{III} removes this ambiguity. At a fixed incident power, the paired channel outputs are further calibrated by an elliptical relation, $(aI_{II} + b)^2 + (cI_{II} + dI_{III} + e)^2 = 1$, allowing the measured (I_{II}, I_{III}) pair to be mapped uniquely to the polarization angle. Channel I therefore determines the incident power, whereas Channels II and III jointly determine the polarization direction, enabling simultaneous electrical readout of these two optical parameters without mechanically rotating the detector or polarization optics.

The subsequent polarization-imaging experiment employs a related but distinct four-channel acquisition scheme. Four 2D β-Ga_2O_3 detectors with the same nominal thickness and size are twistedly stacked to sample photocurrents corresponding

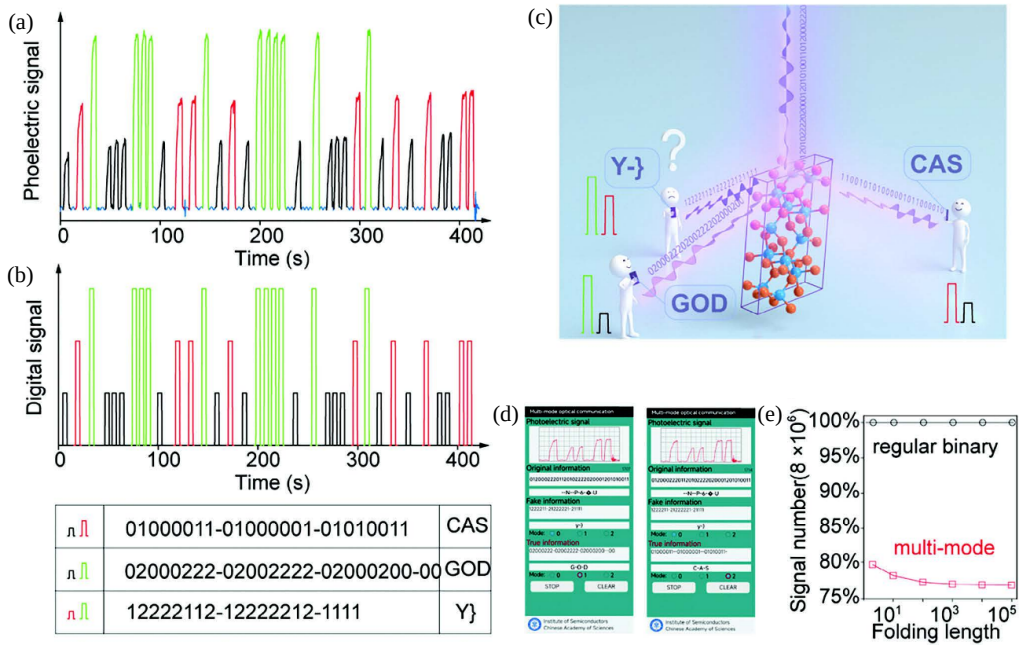

FIGURE 10. Multimode solar-blind ultraviolet communication enabled by the polarization-dependent photocurrent of a β-Ga_2O_3 nanoribbon detector. (a) Polarization-dependent photoelectric signals received by the detector. (b) Digital conversion of the three photocurrent levels into states 0, 1, and 2, together with the corresponding decoding results under different modes. (c) Schematic of the multimode communication strategy based on different combinations of the three digital states. (d) Representative communication interfaces under different decoding modes. (e) Number of digital signals required by conventional binary and multimode communication as a function of folding length, illustrating the reduction in transmitted symbol count achieved by signal sharing [90]. *Reproduced with permission under the terms of the Creative Commons CC BY 4.0 license*.

to 0°, 45°, 90°, and 135° polarization orientations. The first three Stokes parameters are then obtained from $S = I_{0^\circ} + I_{90^\circ}$, $S_1 = I_{0^\circ} - I_{90^\circ}$, $S_2 = I_{45^\circ} - I_{135^\circ}$ and the degree of linear polarization is calculated as DoLP $= \sqrt{(S_1^2 + S_2^2)^2}/S_0$. For the imaging demonstration, a patterned school-badge mask and a scattering medium were placed in the optical path, and the mask platform was scanned pixel by pixel with a step size of 0.067 mm. At each sampling position, the four polarization-dependent photocurrents were collected in one step and converted into DoLP, producing a reconstructed 150 × 150-pixel polarization image. Compared with direct photocurrent imaging from a single β-Ga_2O_3 detector, the DoLP-based image exhibited clearer structural details under the scattering condition (Fig. 9).

These demonstrations illustrate a clear progression from polarization-dependent intensity mapping to quantitative polarization-information reconstruction, but they also reveal the remaining gap between proof-of-concept imaging and an integrated polarimetric imaging system. The 25-pixel array in Ref. [98] distinguishes predefined polarization states through spatial photocurrent contrast but does not reconstruct an unknown polarization state, whereas the scheme in Ref. [99] resolves incident intensity and linear-polarization information through multi-channel calibration and Stokes-parameter analysis. However, the latter remains a scanning single-pixel imaging architecture rather than a monolithic focal-plane array, and its four polarization channels require closely matched detector responses; in the reported demonstration, incident power and bias were adjusted to obtain comparable photocurrent levels and anisotropy ratios among the detectors [99]. For practical imaging, additional system-level metrics — including polarization-angle resolution, Stokes-parameter reconstruction error, channel-to-channel or pixel-to-pixel uniformity, calibration stability, repeatability, and long-term environmental stability — therefore require systematic evaluation. The central challenge for β-Ga_2O_3 polarization imaging is consequently shifting from demonstrating anisotropic photocurrent toward reproducibly mapping that anisotropy into spatially resolved and quantitatively calibrated polarization information.

5. APPLICATION DEMONSTRATIONS AND SYSTEM-LEVEL ASSESSMENT

Having established how the intrinsic anisotropy of β-Ga_2O_3 can be modulated and translated into electrical signals, the next question is what additional functionality this polarization information enables at the application level. Existing demonstrations exploit polarization in fundamentally different roles: as an additional encoding dimension in optical communication, as an optical state variable for neuromorphic processing, as part of the challenge space in physical unclonable functions, and as a detector-side readout dimension in wavelength-assisted molecular sensing. These applications therefore cannot be assessed using a common device figure of merit alone. Instead, their significance depends on how polarization information is encoded, processed, or reconstructed and on whether application-specific requirements such as accuracy, crosstalk, bandwidth, calibration, repeatability, and long-term stability are satisfied. This section examines representative demonstrations from these four

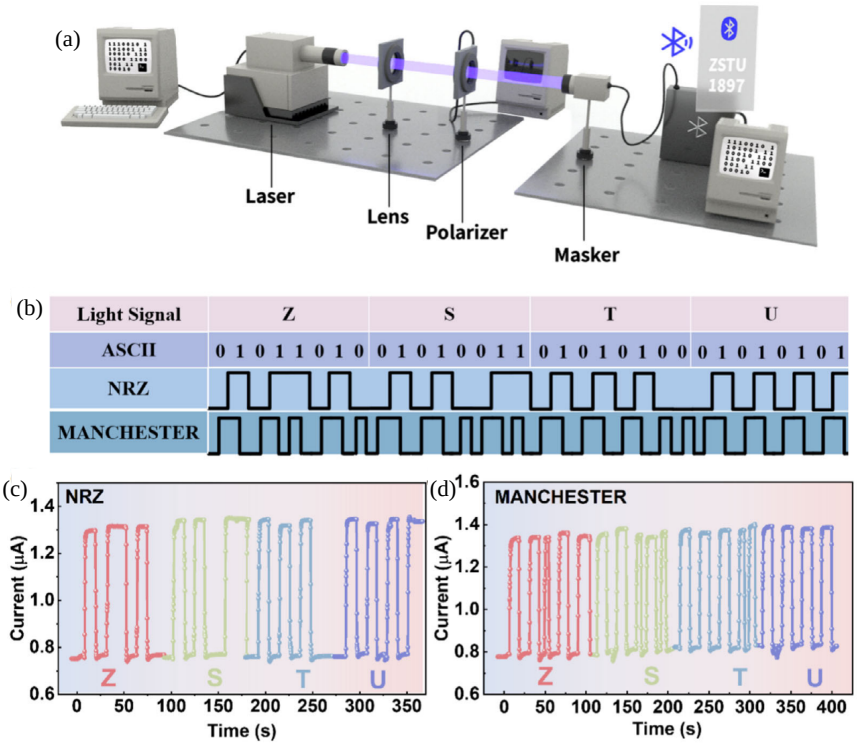

FIGURE 11. Binary solar-blind ultraviolet polarization communication based on an anisotropic β-Ga_2O_3 thin-film photodetector. (a) Schematic configuration of the polarization-sensitive optical communication system. (b) ASCII representation of "ZSTU" and the corresponding NRZ and Manchester encoding waveforms. (c) Experimentally received photocurrent signals for transmission using NRZ encoding. (d) Corresponding transmission using Manchester encoding [35]. *Reproduced with permission under the terms of the Creative Commons CC BY 4.0 license*.

directions while distinguishing proof-of-concept functionality from system-level readiness.

5.1. Polarization-encrypted Optical Communication

Solar-blind ultraviolet communication benefits from the low natural background in the 200–280 nm spectral window, while conventional links commonly encode information through optical intensity or related temporal modulation schemes [101–103]. Introducing polarization provides an additional optical degree of freedom that can be mapped onto distinguishable photocurrent levels or used as a polarization-dependent decoding condition. For β-Ga_2O_3, this functionality is particularly relevant because its intrinsic anisotropic photoresponse enables polarization discrimination without requiring the detector itself to be preceded by a polarization analyzer. Representative demonstrations have therefore explored multilevel and multimode encoding [90], polarization-dependent binary decoding [35], and electronically assisted polarization authentication [104]. The central system-level question, however, is not simply whether different polarization states can generate distinguishable signals, but whether those states remain reliably separable under realistic constraints of noise, bandwidth, polarization misalignment, and channel variability.

Zhao et al. [90] demonstrated how a large polarization contrast can be converted into a multilevel communication alphabet using CVD-grown β-Ga_2O_3 nanoribbon photodetectors. Three light pulses with identical intensity but different polarization angles (θ_1, θ_2, and θ_3) were assigned to three optical states at the transmitter. Owing to the strongly polarization-dependent photocurrent of the β-Ga_2O_3 detector, these states were converted into three distinguishable electrical levels and subsequently digitized as 0, 1, and 2. In this ternary scheme, encoding one character requires five digital symbols instead of eight in a conventional binary representation, corresponding to a 37.5% reduction in the number of symbols and a nominal 1.6-fold increase in information capacity. Simulations incorporating depolarization, angular misalignment, and photoelectric noise further showed that a detector with $PR > 10^3$ can maintain a decoding accuracy above 99% under the assumed error model. The same three-state alphabet was further used for multimode communication (Fig. 10). By selecting different pairs from the three digital states, three binary decoding modes can be defined, allowing an identical transmitted sequence to yield different decoded messages depending on the mode shared by the transmitter and receiver. A separate signal-sharing strategy was also proposed in which adjacent characters share selected digital states; for a large simulated character set, this reduced the required number of transmitted symbols to approximately 77% of that of conventional binary coding, corresponding to an approximately 1.3-fold increase in channel capacity. These two gains should be distinguished: the 1.6-fold value originates from ternary encoding itself, whereas the 1.3-fold value refers to the specific multimode signal-sharing implementation. More importantly, neither value represents a directly measured increase in modulation bandwidth or data rate.

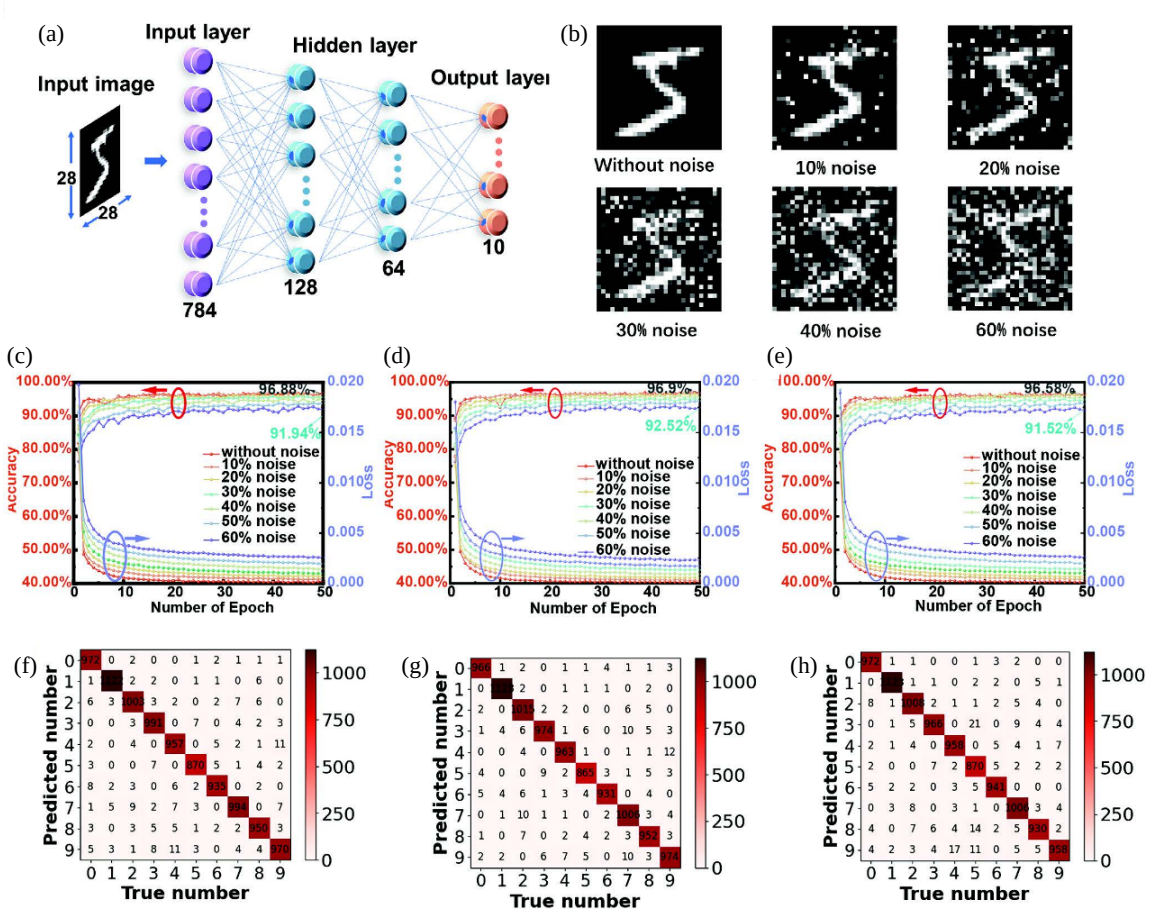

FIGURE 12. Neuromorphic image recognition based on the β-Ga_2O_3 polarization-sensitive optoelectronic synapse. (a) Architecture of the backpropagation neural network for MNIST handwritten-digit recognition. (b) Representative input images with different noise levels. (c)–(e) Recognition accuracy and loss under unpolarized, 90°, and 0° polarized illumination, respectively. (f)–(h) Corresponding confusion matrices after training [106]. *Reproduced with permission under the terms of the Creative Commons CC BY 4.0 license.*

A simpler binary implementation was demonstrated by Wu et al. [35] using highly anisotropic β-Ga_2O_3 thin-film photodetectors grown on r-plane sapphire. The device exhibited a polarization ratio of 6.02 at 254 nm, allowing two polarization-dependent photocurrent levels to be assigned to binary states "1" and "0". Based on this discrimination, the authors demonstrated transmission of the ASCII-encoded message "ZSTU" using both non-return-to-zero (NRZ) and Manchester encoding Fig. 11). In the latter scheme, level transitions provide clock synchronization and improve robustness against low-frequency fluctuations compared with simple NRZ encoding. The detector output was interfaced with a dedicated signal-processing circuit and transmitted to a computer through a serial connection. This demonstration shows that the intrinsic polarization response of β-Ga_2O_3 can function as an additional electrical decoding variable within a conventional binary communication architecture rather than requiring multilevel polarization encoding.

Ni et al. [104] subsequently introduced an electronically assisted polarization-authentication scheme by integrating an off-axis-sapphire β-Ga_2O_3 detector with FPGA-based signal control. The transmitter combined OOK with polarization-angle encoding, whereas the receiver evaluated the angle-dependent photocurrent against predefined thresholds. For each transmitted bit, 80 photocurrent samples were acquired, and a high-level signal was authenticated only when at least 50 samples fell within the prescribed range. Using the ASCII-encoded message "ZSTU", correct recovery was demonstrated when the transmitter and receiver employed the matched polarization sequence (0°, 30°, 60°, and 90°), whereas changing the sequence to 0°, 90°, 60°, and 30° produced erroneous decoding. This approach therefore uses polarization not only as a signal state but also as an additional authentication condition. However, the demonstrated link remained far from high-speed operation: the reported transmission time was approximately 12 s per binary bit and 96 s per English character. Thus, the contribution of the FPGA-based architecture lies primarily in programmable encoding and threshold authentication rather than in a demonstrated increase in communication bandwidth.

Beyond polarization-encoded links, Dong et al. [94] demonstrated that a fully transparent back-illuminated β-Ga_2O_3 detector can also support non-line-of-sight (NLOS) solar-blind UV communication through a scattering channel. In this experiment, information was encoded through LED on/off modulation rather than polarization states, and the received. It signals reproduced the transmitted ASCII patterns in the presence of an optical obstruction. The demonstrated signaling rate remained on the second timescale and was explicitly presented as

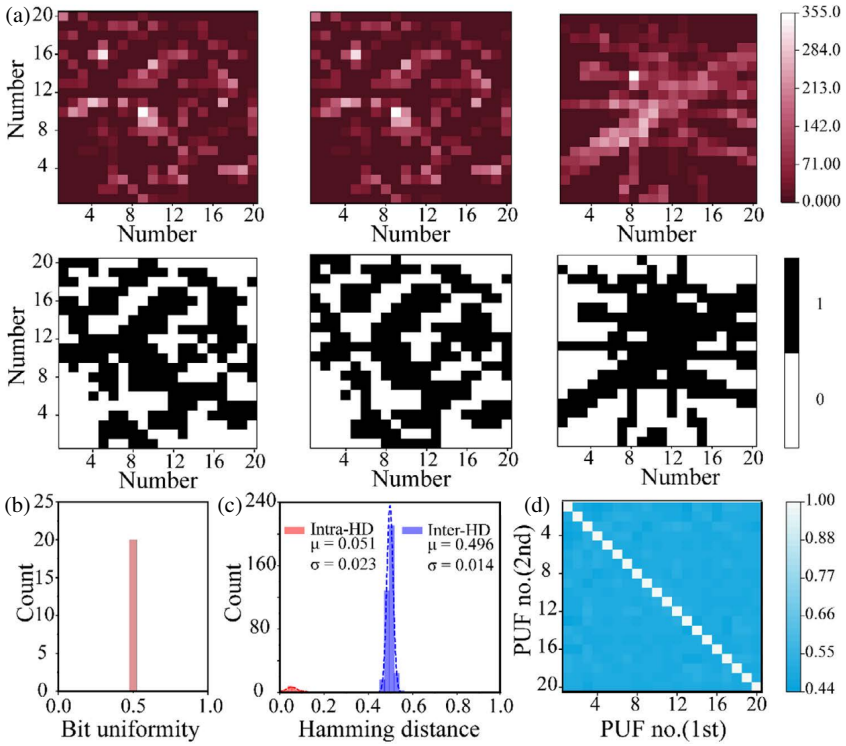

FIGURE 13. Performance evaluation of polarization-sensitive β-Ga_2O_3 microbelt PUFs. (a) Raman mappings and corresponding binary codes obtained from repeated measurements of the same PUF and from a different PUF. (b) Bit uniformity across 20 PUF labels. (c) Distributions of intra- and inter-PUF Hamming distances. (d) Similarity matrix for repeated measurements of the PUF labels [107]. *Reproduced with permission under the terms of the Creative Commons CC BY 4.0 license*.

a proof of concept. Thus, Ref. [94] is relevant here primarily because it extends β-Ga_2O_3 communication toward non-line-of-sight channel conditions, rather than because it demonstrates polarization encryption.

Taken together, these studies demonstrate the feasibility of using β-Ga_2O_3 polarization sensitivity for multilevel encoding, binary decoding, and polarization-assisted authentication, but they remain proof-of-concept communication demonstrations. The $>$ 99% accuracy in Ref. [90] was simulation-based rather than obtained from measured BER, while the links in Refs. [94, 104] operated on the second timescale. Thus, high PR and successful message recovery should not be equated with communication-grade performance. Future work should quantify BER, polarization crosstalk, modulation bandwidth, angular tolerance, and calibration stability under realistic channel conditions.

5.2. Neuromorphic Vision Systems

Polarization-sensitive optoelectronic synapses combine optical sensing with memory and preprocessing functions, allowing polarization information to be processed directly at the device level. β-Ga_2O_3 is particularly suitable for this concept because its intrinsic optical anisotropy provides polarization discrimination, while oxygen-vacancy-related persistent photoconductivity (PPC) can supply the memory effect required for synaptic plasticity [105]. Wang et al. [106] demonstrated such a synapse using a (100)-oriented β-Ga_2O_3 single crystal. Under 254 nm excitation, the device exhibited excitatory postsynaptic current (EPSC), paired-pulse facilitation, and short- to long-term plasticity, with the persistent response attributed to trapping and release of photocarriers associated with oxygen-vacancy-related states. Notably, the EPSC under 0° polarized excitation was approximately 1.6 times that under 90° excitation, enabling polarization-dependent synaptic weighting.

The measured synaptic states were further incorporated into a backpropagation neural network for MNIST handwritten-digit recognition (Fig. 12). After training, recognition accuracies of 96.88%, 96.90%, and 96.58% were obtained under unpolarized, 0°, and 90° polarized conditions, respectively; the accuracy remained above 90% even when 60% noise was introduced. These results demonstrate that polarization-dependent synaptic responses can be incorporated into neuromorphic image-processing architectures, although the similar recognition accuracies among the three polarization conditions also indicate that the quantitative advantage provided specifically by polarization information remains to be established.

These results demonstrate the feasibility of combining polarization sensing with synaptic memory and image processing in a single β-Ga_2O_3 platform. However, the nearly identical MNIST recognition accuracies obtained under unpolarized, 0°, and 90° illumination indicate that the specific computational benefit of polarization information remains to be quantified. Practical neuromorphic vision will further require improved device uniformity, lower operating power, faster processing, and stable integration with array-level readout circuits.

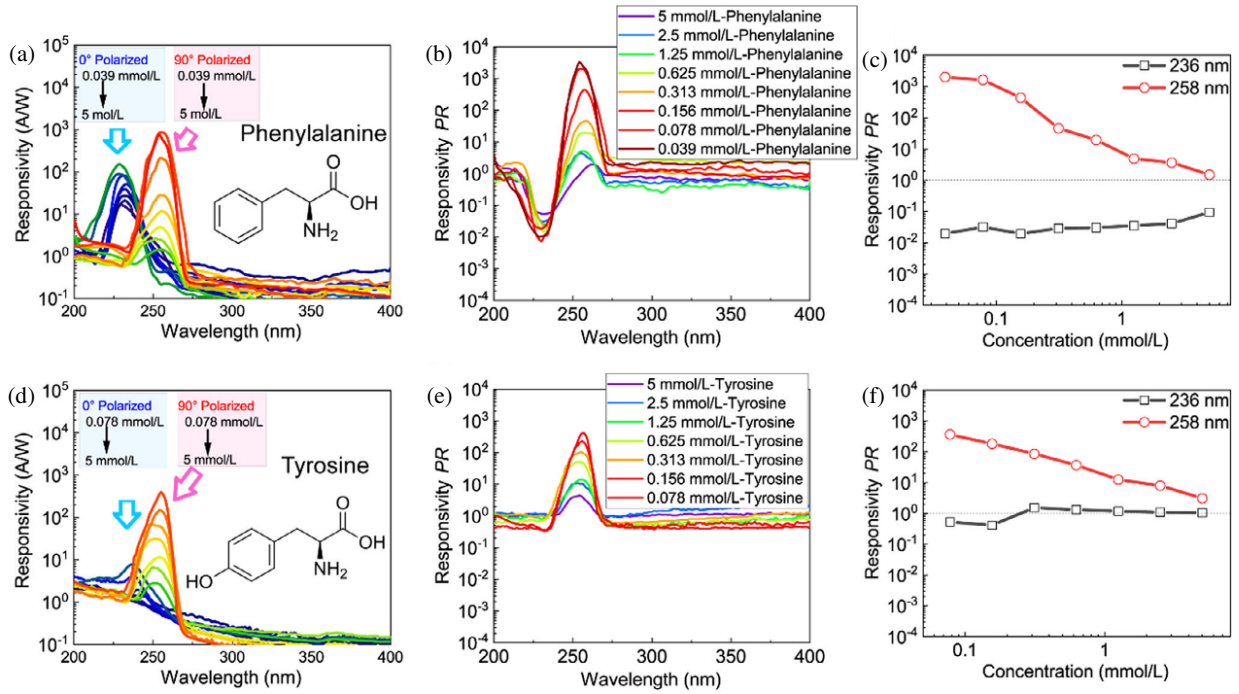

FIGURE 14. Wavelength-polarization-assisted sensing of phenylalanine and tyrosine using a β-Ga_2O_3 photodetector. (a), (d) Photoresponse spectra measured with different concentrations of phenylalanine and tyrosine, respectively. (b), (e) Corresponding directional responsivity-ratio spectra. (c), (f) Directional responsivity ratios at 236 and 258 nm as functions of amino-acid concentration [36]. *Reproduced with permission under the terms of the Creative Commons CC BY 4.0 license.*

5.3. Polarization-encoded Physical Unclonable Functions

Physical unclonable functions (PUFs) exploit random physical variations to generate device-specific authentication responses. Zhang et al. [107] developed a concealable PUF by randomly distributing β-Ga_2O_3 microbelts on a flexible Polydimethylsiloxane (PDMS) substrate and using their polarization-dependent Raman response as the readout signal. Owing to the monoclinic anisotropy of β-Ga_2O_3, the Raman intensity exhibits a periodic dependence on excitation polarization, with the maximum response correlated with the Ga-Ga chain orientation. Raman mappings were converted into binary keys through median-threshold binarization. Across 20 PUF labels, the mean inter-device and intra-device Hamming distances were 0.496 and 0.051, respectively, indicating good uniqueness and repeatability (Fig. 13). More importantly, rotating the excitation polarization by 30° reduced the similarity of the response from the same PUF to approximately 68%, making polarization a hidden challenge parameter rather than merely a readout variable.

The polarization-dependent PUF provides an additional hidden challenge dimension, but its practical implementation remains constrained by Raman-based readout. Precise polarization calibration, spectral instrumentation, and raster mapping increase system complexity and limit authentication throughput. In addition, the incomplete NIST performance of the full key indicates that key-generation robustness requires further improvement before large-scale deployment.

5.4. Wavelength-polarization-assisted Amino Acid Sensing

Zhang et al. [36] demonstrated that the polarization response of β-Ga_2O_3 can vary strongly with detection wavelength because different valence-band transitions obey different polarization selection rules. DFT calculations indicate that $E//c$ primarily drives the $v_{b1} \rightarrow c_{b1}$ transition with a cutoff near 257 nm, whereas $E//b$ mainly excites $v_{b4}/v_{b6} \rightarrow c_{b1}$ transitions with a cutoff near 230 nm. Consistently, the β-Ga_2O_3 microbelt detector exhibited photoresponse maxima near 236 nm for $E//b$ and 258 nm for $E//c$. The dominant polarization direction therefore reverses near 245 nm; using the source-defined directional responsivity ratio $R_{E//c}/R_{E//b}$, the ratio changes from 1/388 at 231 nm to 462 at 263 nm.

This wavelength-dependent anisotropic response was subsequently used for amino-acid sensing. Aqueous phenylalanine and tyrosine solutions were introduced into the optical path as spectrally selective filters. Because phenylalanine and tyrosine exhibit different deep-UV transmittance at 236 and 258 nm, they preferentially attenuate different response bands of the β-Ga_2O_3 detector, producing distinguishable concentration-dependent electrical responses (Fig. 14). Importantly, the amino-acid solutions are optically isotropic: the sensing contrast originates from their wavelength-dependent absorption rather than polarization-selective absorption. Polarization sensitivity is supplied by the β-Ga_2O_3 detector and provides a detector-side readout dimension for the spectrally filtered signal.

Accordingly, this demonstration is more appropriately regarded as wavelength-selective absorption sensing assisted by a polarization-sensitive detector rather than polarization-selective sensing of the amino acids themselves. Although phenylalanine and tyrosine were distinguished in controlled solutions, the additional information provided beyond conventional dual-wavelength UV absorption, as well as specificity,

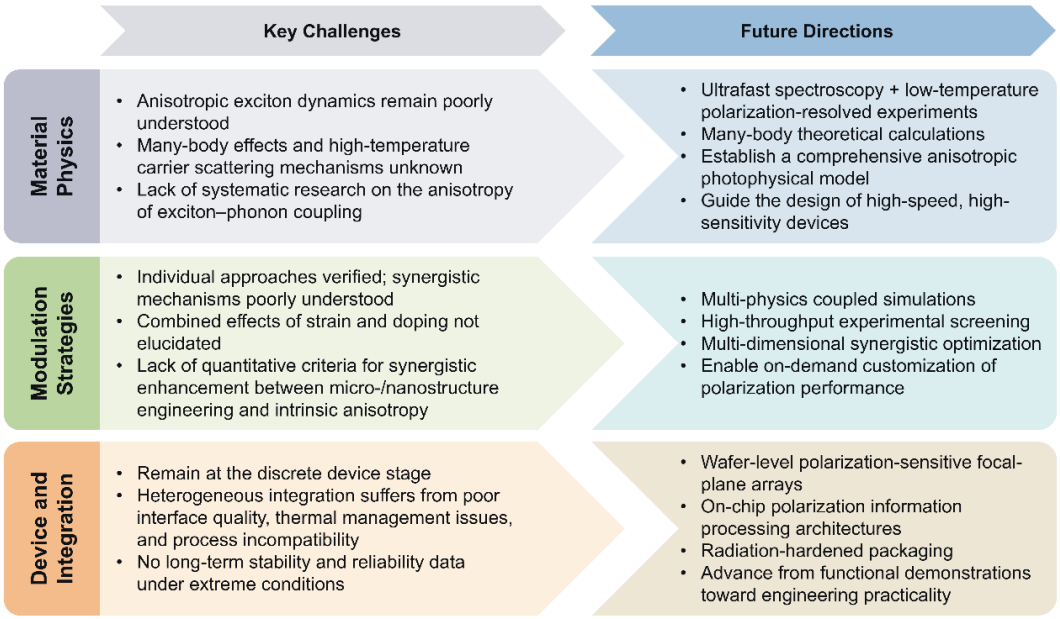

FIGURE 15. Future research roadmap for β-Ga_2O_3 polarization optoelectronics.

detection limits, and interference tolerance in mixed or biological samples, remains to be established.

6. SUMMARY AND PROSPECTS

6.1. Summary

This review has examined β-Ga_2O_3 polarization-sensitive photodetection around a central question: how the intrinsic anisotropy of a low-symmetry ultrawide-bandgap semiconductor can be translated into reliable electrical polarization information. At the materials level, the monoclinic crystal structure produces strongly direction-dependent optical absorption, dielectric response, and excitonic transitions, whereas carrier-transport anisotropy depends more strongly on carrier population and measurement conditions and is generally less pronounced under equilibrium conditions. These microscopic contributions should therefore not be treated as equivalent origins of device polarization sensitivity. External modulation through substrate orientation, strain, doping/alloying, and structural engineering can preserve, reshape, or amplify the intrinsic anisotropy, while artificial gratings can additionally introduce extrinsic polarization selectivity through electromagnetic boundary conditions. The key design problem is consequently not simply to maximize anisotropy, but to identify which physical mechanism dominates the measured polarization response and how efficiently it survives subsequent carrier transport and device readout.

At the device and system levels, β-Ga_2O_3 photodetectors now span high-contrast photoconductive devices, self-powered Schottky and heterojunction architectures, polarization-contrast arrays, and quantitative linear-polarimetric reconstruction. These advances also reveal clear trade-offs: high polarization ratio does not necessarily coincide with high speed, low bias, high responsivity, or accurate polarization reconstruction, while interface engineering may improve carrier extraction without necessarily enhancing — and in some cases while reducing — the original polarization contrast. Application demonstrations in optical communication, neuromorphic processing, physical unclonable functions, and wavelength-assisted molecular sensing further show that device-level anisotropy alone is insufficient to establish system readiness. Across these examples, the recurring bottleneck is the reproducible transfer of microscopic anisotropy through modulation, interfaces, device architecture, calibration, and readout into quantitatively usable polarization information.

6.2. Prospects

Despite substantial progress, the central challenge for β-Ga_2O_3 polarization optoelectronics is no longer simply to obtain a larger polarization ratio, but to understand and control how microscopic anisotropy is transferred into reliable device- and system-level polarization information. Several unresolved questions remain across the material, modulation, and integration scales. As summarized in Fig. 15, these challenges can be grouped into three interconnected levels: Materials Physics, Modulation Strategies, and Device Integration & Applications. Progress at each level will require moving from empirical performance optimization toward quantitative relationships between physical mechanism, polarization response, and information fidelity.

At the Materials Physics level, a key unresolved question is which microscopic processes ultimately determine the magnitude, spectral dispersion, and temporal evolution of the polarization response. Existing studies have established anisotropic dielectric response, excitonic absorption, and direction-dependent carrier dynamics, but the relative contributions of excitonpolariton coupling, free-carrier screening, electron-phonon interactions, and nonequilibrium carrier scattering remain insufficiently quantified across different crystal orientations, doping levels, temperatures, and excitation conditions. Future studies should combine ultrafast

polarization-resolved spectroscopy, low-temperature measurements, and many-body or first-principles calculations to extract axis-dependent carrier lifetimes, scattering rates, screening strengths, and excitonic contributions. The goal should be to establish a predictive microscopic model that connects these quantities directly to wavelength-dependent polarization contrast and temporal response, rather than treating the measured *PR* as an isolated empirical parameter.

At the Modulation Strategies level, the key challenge is to determine whether different engineering approaches act independently, synergistically, or competitively in controlling polarization response. Most existing studies examine substrate orientation, strain, doping/alloying, and micro-/nanostructuring separately, whereas their coupled effects on band structure, defect states, carrier screening, transport, and optical-field distribution remain poorly understood. Future work should therefore establish quantitative design rules for multi-parameter modulation, for example by combining strain with carrier-density control or intrinsic crystallographic anisotropy with nanostructure-induced field engineering. Importantly, any apparent enhancement should be decomposed into its intrinsic and extrinsic contributions so that increased *PR* can be attributed to a defined physical mechanism rather than to an unresolved superposition of effects. Multi-physics simulations combined with systematic high-throughput experiments could provide the parameter maps needed for such mechanism-guided optimization.

At the Device Integration and Applications level, the principal challenge is to translate polarization-sensitive devices into parallel, calibrated, and reliable system architectures. Current demonstrations remain dominated by discrete detectors, small arrays, or scanning-based imaging systems, while wafer-scale polarization-sensitive focal-plane arrays and direct integration with complementary metaloxidesemiconductor (CMOS) readout electronics have yet to be established. Beyond fabrication compatibility and interface quality, practical systems must control pixel-to-pixel and channel-to-channel variation, polarization crosstalk, calibration drift, and reconstruction error. Application-specific metrics — including BER and bandwidth for communication, recognition robustness and energy consumption for neuromorphic systems, authentication throughput for PUFs, and specificity and interference tolerance for molecular sensing — should therefore be evaluated together with conventional device figures of merit. Future development should combine wafer-level fabrication, on-chip polarization reconstruction, standardized calibration protocols, and long-term reliability testing to convert β-Ga_2O_3 anisotropy from a device-level response into reproducible system-level polarization information.

Overall, the next stage of β-Ga_2O_3 polarization optoelectronics should move beyond the pursuit of isolated record metrics toward controlling the fidelity with which microscopic anisotropy is transferred into usable polarization information. Establishing quantitative links among material anisotropy, external modulation, interface-mediated carrier extraction, device readout, and system-level reconstruction will be essential for transforming polarization sensitivity from a material property into a scalable information-processing capability.

ACKNOWLEDGEMENT

This work was supported by the National Natural Science Foundation of China (Nos. 62674208, 62274148, 62304205, and 62374147), the Joint Funds of the National Natural Science Foundation of China (No. U23A20349), the Natural Science Foundation of Hangzhou (No. 2024SZRZDF040001), the Zhejiang Provincial Natural Science Foundation of China (26062044-D), and the Intramural Grant of Zhejiang Sci-Tech University (No. 24062240-Y).

REFERENCES

[1] Sun, Y., Y. Lv, J. Cao, W. Liu, Z. Wang, Y. Mao, and Z. Wang, "Spatial polarization phase shift keying for high-capacity coherent free-space optical communication," *Optics Express*, Vol. 33, No. 25, 51 919–51 935, 2025.

[2] Wang, G., L.-Y. Shao, D. Xiao, S. Bandyopadhyay, J. Jiang, S. Liu, W. Li, C. Wang, and Z. Yan, "Stable and highly efficient free-space optical wireless communication system based on polarization modulation and in-fiber diffraction," *Journal of Lightwave Technology*, Vol. 39, No. 1, 83–90, 2021.

[3] Zhao, Y., Y. Yao, K. Xu, Y. Yang, and J. Tian, "Circular polarization shift-keying modulation based on orbital angular momentum division multiplexing in free space optical communication," *Optics Communications*, Vol. 475, 126165, 2020.

[4] Bielak, M., D. Vašinka, and M. Ježek, "All-fiber microsensor of polarization at single-photon level aided by deep learning," *Laser & Photonics Reviews*, Vol. 20, No. 3, e01775, 2026.

[5] He, X., N. Fujimura, J. M. Lloyd, K. J. Erickson, A. A. Talin, Q. Zhang, W. Gao, Q. Jiang, Y. Kawano, R. H. Hauge, *et al.*, "Carbon nanotube terahertz detector," *Nano Letters*, Vol. 14, No. 7, 3953–3958, 2014.

[6] Yin, C., S. He, X. Fan, Y. Xiao, L. Zhao, and L. Gao, "Gate-modulated and polarization-sensitive photodetector based on the MoS_2/$PdSe_2$ out-of-plane van der Waals heterostructure," *Advanced Optical Materials*, Vol. 12, No. 28, 2401122, 2024.

[7] Yudhistira, Y. and S. Choi, "Compact circular polarization detector with Z-shaped thermoelectric nanoantenna for infrared (IR) polarimetry," *Materials Today Advances*, Vol. 27, 100599, 2025.

[8] Zhou, Y., W. Li, W. Li, X. Huang, C. Dai, Z.-P. Xiao, Z.-P. Li, F. Xu, and J.-W. Pan, "Non-line-of-sight single-pixel imaging using polarization speckle modulation," *Physical Review Letters*, Vol. 136, No. 14, 143801, 2026.

[9] Wang, S., L. Qi, Z. Xia, W. Wang, D. Yue, S. Wang, and S. Su, "Polarization-sensitive detector based on $MoTe_2$/WTe_2 heterojunction for broadband optoelectronic imaging," *The Journal of Physical Chemistry Letters*, Vol. 14, No. 47, 10 509–10 516, 2023.

[10] Chen, J., X. Xu, C. Chen, J. Li, G. Xun, T. Xu, S. Zhang, H. Wu, L. Zhang, D. Guo, *et al.*, "Stable b-AsP/InSe mid-infrared detector with high polarization-sensitivity for target feature discrimination," *Advanced Functional Materials*, Vol. 36, No. 24, e22145, 2026.

[11] Wang, L., J. Zeng, G. Wang, Z. Chen, W. Hu, and Y. Zhang, "Encryption-decryption scheme in a single-pixel system based on polarization and laguerre-gaussian mode modulation," *Optics Express*, Vol. 32, No. 20, 35 438–35 448, 2024.

[12] Liu, C.-Q., C.-H. Zhu, L.-H. Wang, L.-X. Zhang, and C.-X. Pei, "Polarization-encoding-based measurement-device-independent quantum key distribution with a single untrusted source," *Chinese Physics Letters*, Vol. 33, No. 10, 100301,

2016.

[13] Song, C., J. Chen, X. Ding, Y. Xu, H. Xu, H. Li, W. Shen, C. Hu, H. Zhang, S. Wang, and J. Yao, "Ultra-broadband polarization-sensitive O-doped $ZrTe_3$ photodetector induced by UV laser," *Advanced Materials*, Vol. 37, No. 40, 2506840, 2025.

[14] Shi, J., H. Liang, X. Xia, and Q. Abbas, "Band alignment analysis of $CuGaO_2/\beta$-Ga_2O_3 heterojunction and application to deep-UV photodetector," *Applied Surface Science*, Vol. 569, 151010, 2021.

[15] Pan, J., C. Li, H. Geng, Y. Ni, C. Wu, H. Wu, S. Wang, F. Wu, and D. Guo, "Band engineering to suppress dark current in self-powered solar-blind photodetectors for optoelectronics in harsh environments," *Physical Review Applied*, Vol. 24, No. 6, 064043, 2025.

[16] Zhao, X., H. Zhu, K. Chen, Z. Zhu, Z. Fang, W. Tang, Y. Wu, and D. Guo, "Enhanced carrier transport and photoresponse in Ga_2O_3 solar-blind photodetectors via Se-induced valence band modulation," *Advanced Optical Materials*, Vol. 14, No. 2, e02393, 2026.

[17] Yu, Y.-T., X.-Q. Xiang, X.-Z. Zhou, K. Zhou, G.-W. Xu, X.-L. Zhao, and S.-B. Long, "Device topological thermal management of β-Ga_2O_3 Schottky barrier diodes," *Chinese Physics B*, Vol. 30, No. 6, 067302, 2021.

[18] Sheoran, H., S. Fang, F. Liang, Z. Huang, S. Kaushik, N. Manikanthababu, X. Zhao, H. Sun, R. Singh, and S. Long, "High performance of zero-power-consumption MOCVD-grown β-Ga_2O_3-based solar-blind photodetectors with ultralow dark current and high-temperature functionalities," *ACS Applied Materials & Interfaces*, Vol. 14, No. 46, 52 096–52 107, 2022.

[19] Wu, H., J. Pan, C. Wu, J. Wang, C. Jiang, C. Guo, Z. Yu, Z. Wang, S. Du, D. Guo, and J. Hu, "Quantum-confinement-effect-tuned cascade AlQDs/β-Ga_2O_3 heterojunctions for ultrasensitive solar-blind photodetection and interference-resistant imaging," *Small*, Vol. 21, No. 34, 2504173, 2025.

[20] Xiang, X., L.-H. Li, C. Chen, G. Xu, F. Liang, P. Tan, X. Zhou, W. Hao, X. Zhao, H. Sun, *et al.*, "Unintentional doping effect in Si-doped MOCVD β-Ga_2O_3 films: Shallow donor states," *Science China Materials*, Vol. 66, No. 2, 748–755, 2023.

[21] Wu, G., X. Guo, Z. Zhu, H. Song, X. Zhong, J. Wang, and D. Guo, "Dose-dependent γ-ray irradiation damage effects in β-Ga_2O_3 solar-blind deep ultraviolet photodetector," *IEEE Transactions on Electron Devices*, Vol. 72, No. 12, 6814–6821, 2025.

[22] Zhai, K., H. Zhang, S. Li, J. Chen, P. Zhou, H. Cui, D. Pang, Y. Tang, L. Ye, H. Li, *et al.*, "Full-space built-in electric field inside gradient Sn-doped β-Ga_2O_3 photoanodes for enhanced photoelectrochemical solar-blind UV photodetection," *Science China Materials*, Vol. 69, No. 3, 1420–1431, 2026.

[23] Wu, G., X. Guo, F. Zhang, X. Zhong, J. Wang, and D. Guo, "Radiation damage mechanisms in β-Ga_2O_3 MSM solar-blind photodetectors: Insights from proton, neutron, and γ-ray irradiation," *IEEE Electron Device Letters*, Vol. 46, No. 11, 2086–2089, 2025.

[24] Nguyen, H.-D., J.-C. Chen, and T.-H.-T. Nguyen, "Effects of different internal radiation models on heat transfer during Czochralski β-Ga_2O_3 crystal growth," *International Journal of Heat and Mass Transfer*, Vol. 258, 128276, 2026.

[25] Xu, W., Y. Chen, X. Zhou, X. Xu, X. Dong, H. Long, Z. Fang, Z. Yang, D. Chen, H. Qi, and K. H. L. Zha, "Recent advancement and perspective of epitaxial growth and doping of β-Ga_2O_3 thin films for power electronics," *APL Materials*, Vol. 13, No. 10, 100601, 2025.

[26] Jiang, T., H. Wang, H. Zhu, J. Cao, X. Huo, Z. Yang, J. Li, Y. Ma, S. Zhang, X. Xu, and W. Kong, "Single-crystalline β-Ga_2O_3 homoepitaxy on a near van der Waals surface of (100) substrate," *Advanced Science*, Vol. 12, No. 17, 2417436, 2025.

[27] Ye, J., S. Gu, and R. Zhang, "Highly polarized solar-blind ultraviolet polarization photodetector," *Scientia Sinica Physica, Mechanica & Astronomica*, Vol. 55, No. 6, 267331, 2025.

[28] Zheng, Q. Q., L. R. Chen, X. D. Li, K. Ding, D. Pang, H. L. Li, Y. Q. Xiong, H. B. Ruan, L. Fang, W. J. Li, *et al.*, "Boosting the performance of deep-ultraviolet photodetector arrays based on phase-transformed heteroepitaxial β-Ga_2O_3 films for solar-blind imaging," *Science China Technological Sciences*, Vol. 66, No. 9, 2707–2715, 2023.

[29] Wang, L., D. Wang, Z. Chen, T. He, L. Xu, X. Xu, H. Xiao, Y. Zhang, and G. Fang, "Crystal structure prediction of three- and two-dimensional Ga_2O_3 using a multi-objective differential evolution algorithm," *Physical Chemistry Chemical Physics*, Vol. 27, No. 21, 11 393–11 404, 2025.

[30] Bandi, M., V. Zade, S. Roy, A. N. Nair, S. Seacat, S. Sreenivasan, V. Shutthanandan, C. G. Van de Walle, H. Peelaers, and C. V. Ramana, "Effect of titanium induced chemical inhomogeneity on crystal structure, electronic structure, and optical properties of wide band gap Ga_2O_3," *Crystal Growth & Design*, Vol. 20, No. 3, 1422–1433, 2020.

[31] Wu, Z. Y., Z. X. Jiang, C. C. Ma, W. Ruan, Y. Chen, H. Zhang, G. Q. Zhang, Z. L. Fang, J. Y. Kang, and T.-Y. Zhang, "Energy-driven multi-step structural phase transition mechanism to achieve high-quality p-type nitrogen-doped β-Ga_2O_3 films," *Materials Today Physics*, Vol. 17, 100356, 2021.

[32] Verma, D., M. M. R. Adnan, S. Dhara, C. Sturm, S. Rajan, and R. C. Myers, "Anisotropic excitonic photocurrent in β-Ga_2O_3," *Physical Review Materials*, Vol. 7, No. 6, L061601, 2023.

[33] Zhang, Y. and F. Xing, "Anisotropic optical and electric properties of β-gallium oxide," *Journal of Semiconductors*, Vol. 44, No. 7, 071801, 2023.

[34] Mu, W., X. Chen, G. He, Z. Jia, J. Ye, B. Fu, J. Zhang, S. Ding, and X. Tao, "Anisotropy and in-plane polarization of low-symmetrical β-Ga_2O_3 single crystal in the deep ultraviolet band," *Applied Surface Science*, Vol. 527, 146648, 2020.

[35] Zhang, G., Z. Wang, S. Chen, Z. Xi, C. Wu, H. Hu, Z. Liu, F. Wu, S. Wang, Z. Fang, W. Tang, and D. Guo, "Fabrication of highly anisotropic large-area β-Ga_2O_3 thin films via crystal orientation engineering for multifunctional solar-blind polarization-sensitive photodetectors," *Laser & Photonics Reviews*, Vol. 19, No. 20, e00255, 2025.

[36] Zhang, Y., H. Liang, X. Cai, R. Zhu, Y. Zhang, Q. Lu, and Z. Mei, "Transition-rule defined polarization detection of β-Ga_2O_3 for wavelength-dependent sensing of amino acid," *Laser & Photonics Reviews*, Vol. 19, No. 20, e00844, 2025.

[37] Cho, J. B., G. Jung, K. Kim, J. Kim, S.-K. Hong, J.-H. Song, and J. I. Jang, "Highly asymmetric optical properties of β-Ga_2O_3 as probed by linear and nonlinear optical excitation spectroscopy," *The Journal of Physical Chemistry C*, Vol. 125, No. 2, 1432–1440, 2021.

[38] Zhao, M., R. Tong, X. Chen, T. Ma, J. Dai, J. Lian, and J. Ye, "Ellipsometric determination of anisotropic optical constants of single phase Ga_2O_3 thin films in its orthorhombic and monoclinic phases," *Optical Materials*, Vol. 102, 109807, 2020.

[39] Fu, B., Z. Yu, H. Wang, Q. Wang, S. Gao, Y. Qu, X. Zhang, and Y. J. Shi, "Anisotropies of structure, optical properties, contact, and epitaxy on (101)- and (001)-oriented β-Ga_2O_3 crystal planes," *ACS Applied Optical Materials*, Vol. 1, No. 9, 1566–

1574, 2023.

[40] Zhang, K., Z. Xu, J. Zhao, H. Wang, J. Hao, S. Zhang, H. Cheng, and B. Dong, "Anisotropies of angle-resolved polarized Raman response identifying in low miller index β-Ga_2O_3 single crystal," *Applied Surface Science*, Vol. 581, 152426, 2022.

[41] Liu, Z., W. Zhong, L. Gu, H. Wang, L. Li, Z. Xi, Y. Liu, X. Guo, L. Wu, J.-H. Zhang, and W. Tang, "Anisotropic optical properties and polarization-sensitive solar-blind photodetector of polycrystalline Ga_2O_3," *Physica Scripta*, Vol. 100, No. 8, 085927, 2025.

[42] Kluth, E., T. Ogawa, H. Nishinaka, R. Goldhahn, and M. Feneberg, "Absorption anisotropy of orthorhombic single-domain κ-Ga_2O_3 from infrared to ultraviolet: Phonons and bandgaps," *Applied Physics Letters*, Vol. 127, No. 17, 172106, 2025.

[43] Sun, X., W. Wei, F.-F. Ren, S. Gu, R. Zhang, and J. Ye, "Heteroepitaxy and anisotropy of nonpolar m-plane α-$(Al_xGa_{1-x})_2O_3$ films," *Journal of Alloys and Compounds*, Vol. 1016, 178958, 2025.

[44] Sturm, C., J. Furthmüller, F. Bechstedt, R. Schmidt-Grund, and M. Grundmann, "Dielectric tensor of monoclinic Ga_2O_3 single crystals in the spectral range 0.5–8.5 eV," *APL Materials*, Vol. 3, No. 10, 106106, 2015.

[45] Pyatenko, E., J. Vinson, D. Hauschild, C. Wansorra, W. Yang, M. Blum, C. Heske, and L. Weinhardt, "Polarization-dependent resonant inelastic x-ray scattering of β-Ga_2O_3: An experimental and computational study," *APL Materials*, Vol. 13, No. 7, 071110, 2025.

[46] Adnan, M. M. R., D. Verma, C. Sturm, M. Schubert, and R. C. Myers, "Anisotropic Beer-Lambert law in β-Ga_2O_3: Polarization-dependent absorption and photoresponsivity spectra," *Physical Review Applied*, Vol. 21, No. 5, 054059, 2024.

[47] Adnan, M. M. R., M. Schubert, and R. C. Myers, "Origin of the anisotropic Beer-Lambert law from dichroism and birefringence in β-Ga_2O_3," *Applied Physics Letters*, Vol. 125, No. 8, 081103, 2024.

[48] Meissner, M., N. Bernhardt, F. Nippert, B. M. Janzen, Z. Galazka, and M. R. Wagner, "Anisotropy of optical transitions in β-Ga_2O_3 investigated by polarized photoluminescence excitation spectroscopy," *Applied Physics Letters*, Vol. 124, No. 15, 152102, 2024.

[49] Unuma, T., O. Maruyama, K. Yubuta, T. Sugawara, H. Toyota, and A. Kato, "Polarization-resolved broadband dielectric properties of an undoped β-Ga_2O_3 (100) crystal in the visible to terahertz regions," *Optical Materials Express*, Vol. 13, No. 11, 3036–3044, 2023.

[50] Portoff, A., A. Venzie, M. Stavola, W. B. Fowler, and S. J. Pearton, "Determination of dielectric axes and transition moment directions in β-Ga_2O_3 from the polarization dependence of vibrational spectra," *Journal of Applied Physics*, Vol. 127, No. 5, 055702, 2020.

[51] Gopalan, P., S. Knight, A. Chanana, M. Stokey, P. Ranga, M. A. Scarpulla, S. Krishnamoorthy, V. Darakchieva, Z. Galazka, K. Irmscher, *et al.*, "The anisotropic quasi-static permittivity of single-crystal β-Ga_2O_3 measured by terahertz spectroscopy," *Applied Physics Letters*, Vol. 117, No. 25, 252103, 2020.

[52] Ueda, N., H. Hosono, R. Waseda, and H. Kawazoe, "Anisotropy of electrical and optical properties in β-Ga_2O_3 single crystals," *Applied Physics Letters*, Vol. 71, No. 7, 933–935, 1997.

[53] Schewski, R., K. Lion, A. Fiedler, C. Wouters, A. Popp, S. V. Levchenko, T. Schulz, M. Schmidbauer, S. B. Anooz, R. Grüneberg, *et al.*, "Step-flow growth in homoepitaxy of β-Ga_2O_3 (100) — The influence of the miscut direction and faceting," *Apl Materials*, Vol. 7, No. 2, 022515, 2019.

[54] Ma, J., F. Meng, D. Xu, R. Hu, and X. Luo, "Electron mobility and mode analysis of scattering for β-Ga_2O_3 from first principles," *Journal of Physics: Condensed Matter*, Vol. 32, No. 46, 465704, 2020.

[55] Ning, S., S. Huang, Z. Zhang, B. Zhao, R. Zhang, N. Qi, and Z. Chen, "β-Ga_2O_3: A potential high-temperature thermoelectric material," *Physical Chemistry Chemical Physics*, Vol. 24, No. 19, 12 052–12 062, 2022.

[56] Kang, Y., K. Krishnaswamy, H. Peelaers, and C. G. Van de Walle, "Fundamental limits on the electron mobility of β-Ga_2O_3," *Journal of Physics: Condensed Matter*, Vol. 29, No. 23, 234001, 2017.

[57] Wang, Z., K. Cheng, J. Sun, X. Wang, G. Wang, X. Liu, Y. Jia, T. Li, Y. Lei, Z. Wang, H. Chen, and X. Ma, "Ultra-wide bandgap quasi two-dimensional β-Ga_2O_3 with highly in-plane anisotropy for power electronics," *Applied Surface Science*, Vol. 619, 156771, 2023.

[58] Jiang, J., X. Ma, Z. Zhao, S. Yang, and D. Liu, "Three-dimensional anisotropic photoelectric response and carrier transport properties of α-Ga_2O_3 and β-Ga_2O_3," *Physical Review B*, Vol. 112, No. 8, 085205, 2025.

[59] Ho, Y.-C., G. Ye, C. Nnokwe, V. Kuryatkov, J. Warzywoda, L. G. de Peralta, R. He, and A. Bernussi, "Deep ultraviolet optical anisotropy of β-gallium oxide thin films," *ACS Omega*, Vol. 9, No. 26, 27 963–27 968, 2024.

[60] Ma, X., R. Xu, Y. Mei, L. Ying, B. Zhang, and H. Long, "Crystalline anisotropy of β-Ga_2O_3 thin films on a c-plane GaN template and a sapphire substrate," *Semiconductor Science and Technology*, Vol. 37, No. 3, 035003, 2022.

[61] Liu, X., Q. Liu, B. Zhao, Y. Ren, B. W. Tao, and W. L. Zhang, "Comparison of β-Ga_2O_3 thin films grown on r-plane and c-plane sapphire substrates," *Vacuum*, Vol. 178, 109435, 2020.

[62] Yan, S., Z. Ding, X. Zhou, Z. Jia, W. Mu, Q. Xin, X. Tao, and A. Song, "Anisotropic performances and bending stress effects of the flexible solar-blind photodetectors based on β-Ga_2O_3 (100) surface," *Applied Surface Science*, Vol. 610, 155318, 2023.

[63] Zhang, Y., H. Liang, F. Xing, Q. Gao, Y. Feng, Y. Sun, and Z. Mei, "Strain-enhanced polarization sensitivity in β-Ga_2O_3 photodetector," *Science China Physics, Mechanics & Astronomy*, Vol. 67, No. 4, 247312, 2024.

[64] Zeng, H., C. Ma, Y. R. Xue, and M. Wu, "P-type Ca-doped two-dimensional Ga_2O_3 with strain-modulated high hole mobility and anisotropy," *Journal of Physics D: Applied Physics*, Vol. 58, No. 38, 385101, 2025.

[65] Zeng, H., C. Ma, and M. Wu, "Compressively strained p-type Mg-doped two-dimensional Ga_2O_3 with a direct band gap and anisotropic hole mobility," *ACS Applied Nano Materials*, Vol. 8, No. 19, 10 004–10 012, 2025.

[66] Li, P., X. Han, D. Chen, Q. Sai, and H. Qi, "Electrical and optical properties and defects of (100)- and (001)-oriented V-doped β-Ga_2O_3 crystals grown by EFG," *Materials Science in Semiconductor Processing*, Vol. 153, 107159, 2023.

[67] Wang, K., K. Serita, H. Murakami, and M. Tonouchi, "Temperature dependence of anisotropic complex conductivity of β-Ga_2O_3," *Journal of Infrared, Millimeter, and Terahertz Waves*, Vol. 43, No. 7, 612–627, 2022.

[68] Cheng, L., Y. Wu, W. Zhong, D. Chen, H. Qi, and W. Zheng, "Photophysics of β-Ga_2O_3: Phonon polaritons, exciton polaritons, free-carrier absorption, and band-edge absorption," *Journal of Applied Physics*, Vol. 132, No. 18, 185704, 2022.

[69] Li, L., L. Wan, C. Xia, Q. Sai, D. N. Talwar, Z. C. Feng, H. Liu, J. Jiang, and P. Li, "The spatial correlation and anisotropy of β-$(Al_xGa_{1-x})_2O_3$ single crystal," *Materials*, Vol. 16, No. 12, 4269, 2023.

[70] Cooke, J., M. Lou, M. A. Scarpulla, and B. Sensale-Rodriguez, "Polarized photoluminescence from Sn, Fe, and unintentionally doped β-Ga_2O_3," *Journal of Vacuum Science & Technology A*, Vol. 42, No. 2, 022801, 2024.

[71] Wang, J., Z. Chen, X. Ji, Z. Liu, H. Zheng, Y. Liu, S. Li, W. Tang, and P. Li, "Anisotropic Ga_2O_3 nanograting with photonic and band engineering enables high-sensitivity solar-blind photodetectors," *Advanced Optical Materials*, Vol. 13, No. 32, e02309, 2025.

[72] Chen, Q., Y. Zhang, T. Zheng, Z. Liu, L. Wu, Z. Wang, and J. Li, "Polarization detection in deep-ultraviolet light with monoclinic gallium oxide nanobelts," *Nanoscale Advances*, Vol. 2, No. 7, 2705–2712, 2020.

[73] Zhang, Y., Y. Zhang, H. Liang, R. Zhu, X. Wang, X. Peng, and Z. Mei, "Enabling DUV polarization detection with isotropic amorphous gallium oxide," *The European Physical Journal Special Topics*, Vol. 234, No. 2, 311–317, 2025.

[74] Zhang, Y., Z. Wang, and F. Xing, "Enhancement of polarization response in UVA and UVC wavelength with integrated subwavelength metal-grids," *Microelectronic Engineering*, Vol. 242-243, 111555, 2021.

[75] Jia, W., M. Lou, P. Gopalan, A. Bhattacharyya, S. Krishnamoorthy, and B. Sensale-Rodriguez, "On the terahertz response of metal-gratings on anisotropic dielectric substrates and its prospective application for anisotropic refractive index characterization," *Journal of Applied Physics*, Vol. 131, No. 19, 193101, 2022.

[76] Wu, G., Y. Xu, Y. Weng, F. Wu, and D. Guo, "Achieving programmable bipolar photocurrents via *p-n* junction design for PEPS-based optoelectronic applications," *Applied Physics Letters*, Vol. 128, No. 11, 113305, 2026.

[77] Xu, S., C. Li, Y. Yang, C. Tian, X. Peng, H. Long, M. Hong, and W. Yang, "Bond-angle modulation in the nucleation layer overcomes the lattice-mismatch limits in Ga_2O_3 heteroepitaxy," *Materials Futures*, Vol. 5, No. 3, 035701, 2026.

[78] Wu, G., K. Chen, Y. Ni, C. Wu, J. Liu, H. Hu, X. Zhang, S. Wang, F. Wu, Z. Wu, and D. Guo, "High responsivity, ultraflexible, self-driven solar-blind fibrous photoelectrochemical detector for seawater antibiotic detection," *Materials Today Physics*, Vol. 53, 101702, 2025.

[79] Pei, X. Y., S. H. Gu, F.-F. Ren, D. W. Yan, Y. Yang, S. L. Gu, R. Zhang, and J. D. Ye, "Quantitative insight into illumination-induced barrier lowering mediated by self-trapped-holes in Ga_2O_3 Schottky photodiodes," *Applied Physics Letters*, Vol. 128, No. 11, 112104, 2026.

[80] Jin, S., Y. Weng, H. Xu, M. A. Iqbal, K. Chen, A. Chen, and D. Guo, "Solar-blind deep ultraviolet photoelectrochemical detectors: Materials, mechanisms, and applications," *Materials Today Physics*, Vol. 59, 101869, 2025.

[81] Zhou, S., L. Chen, A. Yan, H. Zhang, Y. Tang, D. Pang, H. Li, L. Ye, P. Yu, and W. Li, "Voltage-tunable graphene/β-Ga_2O_3 heterojunction solar-blind photodetector enabling photovoltaic and photoconductive dual-mode operation," *Optics Letters*, Vol. 51, No. 1, 221–224, 2026.

[82] Liu, N., T. Zhang, L. Chen, J. Zhang, S. Hu, W. Guo, W. Zhang, and J. Ye, "Fast-response amorphous Ga_2O_3 solar-blind ultraviolet photodetectors tuned by a polar AlN template," *IEEE Electron Device Letters*, Vol. 43, No. 1, 68–71, 2022.

[83] Wang, Z., F. Zhang, T. Sun, X. Liu, Y. Peng, Z. Chen, P. Wangyang, D. Guo, X. Wang, and H. Li, "Effect of deposition temperature on the characteristics of Ga_2O_3 films grown on flexible mica and the performance of corresponding photodetectors," *ACS Applied Optical Materials*, Vol. 3, No. 2, 272–283, 2025.

[84] Wu, H., J. Pan, J. Wang, C. Guo, S. Du, D. Xiao, D. Guo, and J. Hu, "Pyro-phototronic-enhanced self-powered broadband UV photodetector based on GaNQDs/GaN homojunction for deep-UV imaging applications," *Materials Today Physics*, Vol. 58, 101876, 2025.

[85] Kang, Q., A. Liu, S. Jiao, S. Liu, M. Luo, W. Gao, H. Wang, Q. Zhao, H. Ge, T. Zhao, *et al.*, "Phonon-polaritonic long-wavelength infrared photodetectors," *Optics Express*, Vol. 34, No. 7, 12014, 2026.

[86] Hua, Y., L. Tang, C. Xia, K. Fang, X. Zhang, W. Lu, J. Nong, and W. Wei, "Self-powered polarization-sensitive photodetector enabled by b-AsP/Ta_2NiS_5/$PtSe_2$ van der Waals heterostructure," *Advanced Optical Materials*, Vol. 14, No. 11, e03232, 2026.

[87] Xiong, H., Y. Cheng, Z. Xu, H. Wu, and S. Qiu, "Physical model and experimental results for millimeter-wave emissivity of seawater foam at W-band," *IEEE Transactions on Geoscience and Remote Sensing*, Vol. 64, 1–16, 2026.

[88] Li, M., S. Yan, M. Li, Z. Xi, S. Li, Z. Zhang, M. Xu, L. Yang, and W. Tang, "Co-doping improves memory characteristics in InSn-Ga_2O_3 detector via multiple impurity energy levels," *Science China Technological Sciences*, Vol. 68, No. 10, 2020901, 2025.

[89] Chen, H., X. Zhao, X. Liu, Q. Lu, S. Wang, Z. Wang, Y. Jia, Y. Guan, L. Li, and Y. Hao, "β-Ga_2O_3 solar-blind ultraviolet light detector with infinite PDCR," *Science China Information Sciences*, Vol. 68, No. 4, 140403, 2025.

[90] Zhao, K., J. Yang, P. Wang, Z. Zhou, H. Long, K. Xin, C. Liu, Z. Han, K. Liu, and Z. Wei, "β-Ga_2O_3 nanoribbon with ultrahigh solar-blind ultraviolet polarization ratio," *Advanced Materials*, Vol. 36, No. 46, 2406559, 2024.

[91] Long, H., T. Xiong, J. Hu, K. He, Y. Liu, J. Yang, and Z. Wei, "Solar-blind ultraviolet anisotropic polarization detection by β-Ga_2O_3 based Schottky photodiodes," *IEEE Electron Device Letters*, Vol. 45, No. 7, 1153–1156, 2024.

[92] Li, L., S. Yao, Y. Wang, X. Meng, J.-H. Zhang, S. Zhang, J. Huang, D. Guo, S. Li, X. Ji, W. Tang, and Z. Liu, "Fermi-level pinning-free 2D hybrid MXene/β-Ga_2O_3 van der Waals polarization-sensitive Schottky photodiodes," *Laser & Photonics Reviews*, Vol. 20, No. 7, e02467, 2026.

[93] Chen, X., W. Mu, Y. Xu, B. Fu, Z. Jia, F.-F. Ren, S. Gu, R. Zhang, Y. Zheng, X. Tao, and J. Ye, "Highly narrow-band polarization-sensitive solar-blind photodetectors based on β-Ga_2O_3 single crystals," *ACS Applied Materials & Interfaces*, Vol. 11, No. 7, 7131–7137, 2019.

[94] Dong, D., J. Wang, X. Xu, M. Peng, Z. Wang, C. Wang, and Z. Wu, "Construction of a fully transparent β-Ga_2O_3 multimode solar-blind detection experimental system based on back incidence technology," *Acta Physica Sinica*, Vol. 74, No. 22, 104–114, 2025.

[95] Li, L., S. Yan, W. Ma, J.-H. Zhang, S. Zhang, M. Jiang, L. Gao, W. Tang, and Z. Liu, "Angle-resolved polarization Raman spectroscopy of β-Ga_2O_3 and their application in sensitive solar-blind photodetection," *Applied Physics Letters*, Vol. 125, No. 14, 141102, 2024.

[96] Zhao, B., C. Wu, H. Wu, F. Wu, S. Wang, and D. Guo, "β-Ga_2O_3 microwire solar-blind photodetectors with high polar-

ization ratio for multifunctional information encryption," *Advanced Optical Materials*, Vol. 13, No. 33, e02580, 2025.

[97] Wu, C., G. Zhang, J. Jia, H. Hu, F. Wu, S. Wang, and D. Guo, "Highly polarization-deep-ultraviolet-sensitive β-Ga_2O_3 epitaxial films by disrupting rotational symmetry and encrypted solar-blind optical communication application," *The Journal of Physical Chemistry Letters*, Vol. 15, No. 14, 3828–3834, 2024.

[98] Gu, Y.-J., S. Li, Y.-X. Wang, J.-Q. Lu, Q.-C. Zhan, Y. Jiang, X.-Q. Ji, and W.-H. Tang, "Solar-blind UV photodetector based on anisotropic Ga_2O_3/MgO heteroepitaxial structure for polarization imaging," *IEEE Transactions on Electron Devices*, Vol. 73, No. 2, 995–1000, 2026.

[99] Zhong, W., H. Huang, Y. Liu, J. Jing, W. Wu, W. Liu, X. Zhao, S. Long, and H. Xu, "Liquid-metal-assisted exfoliation of 2D β-Ga_2O_3 with high anisotropy ratio for solar-blind detection and polarization imaging," *Applied Physics Reviews*, Vol. 12, No. 1, 011420, 2025.

[100] Mudiyanselage, D. H., R. Mandia, D. Wang, J. Adivarahan, Z. He, K. Fu, Y. Zhao, M. R. McCartney, D. J. Smith, and H. Fu, "Anisotropic electrical properties of NiOx/β-Ga_2O_3 *p-n* heterojunctions on $(\bar{2}01)$, (001), and (010) crystal orientations," *Applied Physics Express*, Vol. 16, No. 9, 094002, 2023.

[101] Ye, J., S. Jin, Y. Cheng, H. Xu, C. Wu, F. Wu, and D. Guo, "Photocurrent ambipolar behavior in phase junction of a Ga_2O_3 porous nanostructure for solar-blind light control logic devices," *ACS Applied Materials & Interfaces*, Vol. 16, No. 20, 26 512–26 520, 2024.

[102] Xu, H., L. Deng, Y. Cheng, C. Wu, K. Chen, and D. Guo, "Regulating photocurrent polarity reversal point in α-Ga_2O_3 nanorod arrays for combinational logic circuit applications," *ACS Applied Nano Materials*, Vol. 7, No. 2, 2359–2369, 2024.

[103] Xu, H., Y. Weng, K. Chen, C. Wu, H. Hu, and D. Guo, "Ultra-low BER encrypted communication based on self-powered bipolar photoresponse ultraviolet photodetector," *Advanced Optical Materials*, Vol. 13, No. 4, 2402238, 2025.

[104] Ni, Z., X. Zhang, C. Niu, J. Niu, C. Wu, D. Guo, and S. Wang, "Substrate engineering of β-Ga_2O_3 thin films on off-axis sapphire for polarization-sensitive solar-blind UV photodetector and encrypted communication," *IEEE Sensors Journal*, Vol. 25, No. 17, 32 530–32 535, 2025.

[105] Wang, Z., C. Wu, F. Wu, D. Guo, and S. Wang, "Polarization-modulated solar-blind optoelectronic synapse based on anisotropic β-Ga_2O_3 crystal for logic operations and motion perception," *ACS Photonics*, Vol. 12, No. 9, 5291–5301, 2025.

[106] Wang, Z., G. Zhang, X. Zhang, C. Wu, Z. Xia, H. Hu, F. Wu, D. Guo, and S. Wang, "Polarization-sensitive artificial optoelectronic synapse based on anisotropic β-Ga_2O_3 single crystal for neuromorphic vision systems and information encryption," *Advanced Optical Materials*, Vol. 12, No. 29, 2401256, 2024.

[107] Zhang, Z.-F., F.-H. Jiao, X. Yang, C.-N. Lin, Y.-W. Hu, W.-B. Zhao, Y.-N. Wang, H.-R. Zheng, L. Dong, and C.-X. Shan, "Concealable physical unclonable functions based on polarization-sensitive Raman scattering," *Laser & Photonics Reviews*, Vol. 20, No. 1, e01264, 2026.

[108] Xu, J., W. Zheng, and F. Huang, "Gallium oxide solar-blind ultraviolet photodetectors: A review," *Journal of Materials Chemistry C*, Vol. 7, No. 29, 8753–8770, 2019.

[109] Tang, H., B. Lou, F. Du, G. Gao, M. Zhang, X. Ni, E. Hu, A. Yacoby, Y. Cao, S. Fan, and E. Mazur, "An adaptive moiré sensor for spectro-polarimetric hyperimaging," *Nature Photonics*, Vol. 19, No. 5, 463–470, 2025.

[110] Fan, Y., W. Huang, F. Zhu, X. Liu, C. Jin, C. Guo, Y. An, Y. Kivshar, C.-W. Qiu, and W. Li, "Dispersion-assisted high-dimensional photodetector," *Nature*, Vol. 630, No. 8015, 77–83, 2024.

[111] Chen, Y., Y. Wang, Z. Wang, Y. Gu, Y. Ye, X. Chai, J. Ye, Y. Chen, R. Xie, Y. Zhou, *et al.*, "Unipolar barrier photodetectors based on van der Waals heterostructures," *Nature Electronics*, Vol. 4, No. 5, 357–363, 2021.

[112] Wang, Y., Y. Tang, H. Li, Z. Yang, Q. Zhang, Z. He, X. Huang, X. Wei, W. Tang, W. Huang, and Z. Wu, "p-GaSe/*n*-Ga_2O_3 van der Waals heterostructure photodetector at solar-blind wavelengths with ultrahigh responsivity and detectivity," *ACS Photonics*, Vol. 8, No. 8, 2256–2264, 2021.

[113] Su, J., X. Chen, L. Shi, B. Niu, J. Chang, J. Zhang, and Y. Hao, "Triple modulation of MoS_2/β-Ga_2O_3 van der Waals heterojunction on the response performance of β-Ga_2O_3 deep ultraviolet photodetector," *ACS Photonics*, Vol. 12, No. 2, 847–854, 2025.

[114] Yu, Z., J. Shen, Y. Ni, S. Wang, F. Wu, D. Guo, and C. Wu, "High performance solar-blind UV photodetector based on C_8-BTBT/β-Ga_2O_3 core-shell structure *pn* heterojunction," *ACS Applied Electronic Materials*, Vol. 7, No. 11, 5100–5105, 2025.

[115] Chen, S., Z. Ni, Y. Xu, Z. Yu, Z. Zhu, D. Guo, and C. Wu, "Fabrication of a self-powered β-Ga_2O_3/PEDOT:PSS heterojunction for polarization-sensitive ultraviolet imaging sensing," *ACS Applied Electronic Materials*, Vol. 8, No. 8, 3591–3598, 2026.

[116] Elameen, A. A. A., D. Dutta, S. Duman, M. Rosmus, G. D'Olimpio, B. Gürbulak, D. W. Boukhvalov, A. Agarwal, and A. Politano, "Electronic band structure of gallium sulfide (GaS) with thickness reduction unveiling parabolic and pudding mold band dispersion," *The Journal of Physical Chemistry C*, Vol. 129, No. 7, 3967–3974, 2025.

[117] Boukhvalov, D. W., G. D'Olimpio, T. Dadiani, J. Sharma, A. A. A. Elameen, S. Zenone, M. Rosmus, B. Gürbulak, E. Cepni, E. Llobet, *et al.*, "Self-assembled gallium sulfide (GaS) heterostructures enabling efficient water splitting and selective ammonia sensing," *Advanced Functional Materials*, Vol. 35, No. 47, 2507388, 2025.

[118] Moore, A., S. Rafique, C. Llewelyn, D. Lamb, and L. Li, "A review of Ga_2O_3 heterojunctions for deep-UV photodetection: Current progress, methodologies, and challenges," *Advanced Electronic Materials*, Vol. 11, No. 9, 2400898, 2025.

[119] Zhu, X., Y. Wu, Z. Pan, and W. Lu, "Advancements in Ga_2O_3-based heterojunction ultraviolet photodetectors: Types, fabrication techniques, and integrated materials for enhancing photoelectric conversion efficiency," *Journal of Alloys and Compounds*, Vol. 1010, 177757, 2025.

[120] Gutiérrez, Y., S. Dicorato, E. Dilonardo, F. Palumbo, M. M. Giangregorio, and M. Losurdo, "Stability of nanometer-thick layered gallium chalcogenides and improvements via hydrogen passivation," *ACS Applied Nano Materials*, Vol. 6, No. 21, 20 161–20 172, 2023.

[121] Cottam, N. D., B. T. Dewes, M. Shiffa, T. S. Cheng, S. V. Novikov, C. J. Mellor, O. Makarovsky, D. Gonzalez, T. Ben, and A. Patanè, "Thin Ga_2O_3 layers by thermal oxidation of van der Waals GaSe nanostructures for ultraviolet photon sensing," *ACS Applied Nano Materials*, Vol. 7, No. 15, 17 553–17 560, 2024.

[122] Al Mutairi, A. A., A. Xhameni, X. Guo, I. Chircă, V. Nicolosi, S. Hofmann, and A. Lombardo, "Controlled fabrication of native ultra-thin amorphous gallium oxide from 2D gallium sulfide for emerging electronic applications," *Advanced Materials Interfaces*, Vol. 12, No. 1, 2400481, 2025.